Journal of Materials Chemistry A

ROYAL SOCIETY OF CHEMISTRY

PAPER

View Article Online
View Journal | View Issue

Check for updates

Cite this: *J. Mater. Chem. A*, 2024, **12**, 7605

Uncovering the critical function of lanthanum in CH_4 production from CO_2 using exsolved $LaNiO_3$ perovskite catalysts†

Mathias Barreau,*[a] Davide Salusso,[b] Jinming Zhang,[a] Michael Haevecker,[cd] Detre Teschner,[cd] Anna Efimenko,[ef] Fabrice Bournel,[gh] Jean-Jacques Gallet,[gh] Elisa Borfecchia,[i] Kamil Sobczak,[j] Corinne Petit[a] and Spyridon Zafeiratos*[a]

CO_2 methanation, also known as the Sabatier reaction, is of great environmental interest as a sustainable process for energy production and storage. Herein, we report the development of a Ni–La_2O_3 catalyst for CO_2 methanation prepared upon reduction of a $LaNiO_3$ perovskite precursor. The perovskite-based catalyst exhibits enhanced activity, high methane selectivity and improved stability when compared to Ni–La_2O_3 prepared through conventional impregnation methods. The transformation of the $LaNiO_3$ perovskite precursor upon thermal activation in H_2 was found to have a profound impact on the catalytic properties of the resulting material. The size and stability of exsolved Ni nanoparticles after prolonged reaction were investigated using *ex situ* electron microscopy. Synchrotron-based X-ray absorption fine structure (XAFS) spectroscopy, as well as soft and tender X-ray photoelectron spectroscopies (AP-XPS/HAXPES), provides detailed insights into the evolution of bulk and surface phases during the transition of the perovskite to its active catalytic state. Our findings indicate that processes beyond the well-established exsolution of nanoparticles, such as lanthana spillover onto nickel, may occur during H_2 activation. More importantly, *in situ* spectroscopy under CO_2 methanation conditions revealed that the surface's affinity for La-hydroxide or La-carbonate formation significantly influences the reactivity. Specifically, we found that La-hydroxide acts as a precursor for the formation of La-oxycarbonate (hexagonal $La_2O_2CO_3$ phase), a crucial element of the active exsolved catalyst. In contrast, in the absence of La-hydroxide, La-carbonates ($La_2(CO_3)_3$) formed on the surface, blocking the active sites of the supported catalyst. Our research examines hitherto unrecognized processes affecting the reactivity of exsolved perovskites, highlighting $LaNiO_3$ as a promising catalyst for CO_2 methanation.

Received 29th November 2023
Accepted 13th February 2024

DOI: 10.1039/d3ta07391b

rsc.li/materials-a

1. Introduction

Global warming caused by the emission of greenhouse gases has attracted a lot of attention during the last few decades. In this context, CO_2, a major component of the anthropogenic emissions (estimated to 35 Gt in 2021 (ref. 1 and 2)), can be captured and used as a carbon source to produce value added chemicals and fuels such as methanol, CO or CH_4.[3,4] Among the most viable strategies, CO_2 methanation ($CO_2 + 4H_2 \rightarrow CH_4 + 2H_2O$) is gaining increasing interest[5,6] as a promising route to recycle CO_2 emissions using H_2 produced from renewable energies (known as power-to-gas). Highly active CO_2 methanation catalysts are required to overcome the chemical inertness of the CO_2 molecule. Among them Ni,[7–9] Co[10–12] or Ru-based[13,14]

[a]*Institut de Chimie et Procédés pour l'Energie, l'Environnement et la Santé (ICPEES), ECPM, UMR 7515 CNRS – Université de Strasbourg, 25 rue Becquerel, Cedex 02, 67087 Strasbourg, France. E-mail: mathias.barreau@unicaen.fr; spiros.zafeiratos@unistra.fr*

[b]*European Synchrotron Radiation Facility, CS 40220, Cedex 9 F-38043 Grenoble, France*

[c]*Max-Planck-Institut für Chemische Energiekonversion (MPI-CEC), Stiftstrasse 34-36, D-45470 Mülheim a.d. Ruhr, Germany*

[d]*Fritz-Haber-Institut der Max-Planck-Gesellschaft, Faradayweg 4-6, D-14195 Berlin, Germany*

[e]*Interface Design, Helmholtz-Zentrum Berlin für Materialien und Energie GmbH (HZB), Albert-Einstein-Str. 15, 12489 Berlin, Germany*

[f]*Energy Materials In-situ Laboratory Berlin (EMIL), Helmholtz-Zentrum Berlin für Materialien und Energie GmbH (HZB), Albert-Einstein-Str. 15, 12489 Berlin, Germany*

[g]*Laboratoire de Chimie Physique-Matière et Rayonnement, Sorbonne Universite, Campus Curie, CNRS UMR 7614, 4 place Jussieu, 75005 Paris, France*

[h]*Synchrotron SOLEIL, L'orme des Merisiers, B.P. 48, Saint Aubin, Gif-sur-Yvette Cedex 91192, France*

[i]*Department of Chemistry, INSTM Reference Center and NIS Centers, University of Torino, 10125 Torino, Italy*

[j]*Faculty of Chemistry, Biological and Chemical Research Centre, University of Warsaw, Zwirki, Wigury 101, 02-089 Warsaw, Poland*

† Electronic supplementary information (ESI) available. See DOI: https://doi.org/10.1039/d3ta07391b

supported catalysts have been reported as active and selective for the production of CH_4 from CO or CO_2. Notably, Ni-based catalysts are mostly envisaged for the reaction because of their low price and high CH_4 selectivity therefore they are more favorable for industrial applications.[6] However, Ni exhibits relatively poor activity at low temperature in comparison to Ru-based catalysts and is often subject to deactivation mainly caused by Ni particle sintering and/or poisoning.[15,16] Consequently, an improvement in the catalyst formulation is needed to elevate CO_2 methanation as one of the major green industrial processes.

Typically, nickel-based methanation catalysts are composed of nanosized Ni particles fixed on high surface area oxide supports, such as Al_2O_3, SiO_2 or CeO_2.[17] The support controls the dispersion, morphology and/or structure of nickel particles *via* metal–support interactions.[18,19] It might also have significant influence on the reactivity by structure-sensitivity effects[20] or by directly participating in the reaction offering sites for CO_2 adsorption and activation.[7,21] Basic elements such as La and Pr have been used as promoters to increase Ni dispersion and help limit deactivation over CeO_2- or Al_2O_3-based materials.[22,23] While poorly studied, Ni supported over La_2O_3 (lanthana) was found to be a promising methanation catalyst mainly due to the stabilization of Ni nanoparticles and limited sintering.[24] However, lanthanum-supported catalysts still suffer from relatively poor activity compared for instance to ceria-based materials.[25]

Stabilization of nickel nanoparticles on a support is not trivial, as nickel undergoes agglomeration easily, which ends up degrading the catalyst performance. In this context, exsolution has received a lot of attention over the last decade as a promising approach to synthesize supported metallic catalysts with specific characteristics.[26–28] Exsolution, also known as solid phase crystallization, is a process by which a homogeneous phase is separated into two or more solid phases typically upon annealing at high temperature.[29–31] In the case of mixed oxides under reductive conditions, one or more elements will move outwards forming metallic nanoparticles at the oxide surface leading to a morphology resembling that of supported metal catalysts. Exsolution, as opposed to traditional deposition procedures, may offer better control of the metal–support interface.[26,27,29] Additionally, exsolved metal nanoparticles usually show strong anchoring to the host oxide (also called socketing) enhancing in this way metal–support interaction and stability.[26,27,29,32]

Perovskite-based materials (ABO_3) containing Ni in the B-site are frequently used as precursors which after a thermal reduction treatment will release Ni from the oxide lattice to the surface in the form of metallic nanoparticles leaving behind the host lattice as the support. So far, numerous combinations of stoichiometric, but mostly A or B-site deficient, perovskite systems have been studied with the main aim of favoring the exsolution of Ni and controlling the nature of the "support" phase. Among all, the stoichiometric $LaNiO_3$ perovskite is the archetype of exsolved materials because it is easy to synthesize, has a relatively simple chemistry upon reduction and above all represents an excellent catalyst for CO_2 conversion.[31] It is therefore not surprising that $LaNiO_3$ is probably the most studied exsolved catalyst in the literature, both in terms of physicochemical and catalytic properties. However, the great majority of these studies focus on CO_2 conversion *via* dry methane reforming[33] and it is hard to find reports on the performance and chemistry of $LaNiO_3$ in the CO_2 methanation reaction. This is even more intriguing if one considers the radically different operation conditions between dry reforming and methanation of CO_2 dictated by the thermodynamics of the reaction: high temperature (*ca.* 800 °C) and pressure for reforming, medium temperature (*ca.* 350 °C) and atmospheric pressure for methanation. Considering that the active catalytic state is dynamic and is formed only under the operation conditions,[34] significant differences in the chemistry of the catalysts should be anticipated in the two cases.

Rare studies over A-deficient perovskites have shown that exsolved Ni catalysts can also be very promising for CO_2 hydrogenation. Suk Lim *et al.* evaluated Ni-exsolved $La_{1-x}Ca_x$-NiO_3 perovskites as methanation catalysts after reduction pretreatment at 600 °C.[35] The resulting material showed nearly 100% CH_4 selectivity and the yield improved by 45% in comparison to the conventional Ni/Al_2O_3 catalyst with similar Ni loading. Steiger *et al.* prepared $LaFe_{0.8}Ni_{0.2}O_3$ perovskite modified in the A-site by Sr doping for CO_2 hydrogenation.[36] They found by *in situ* XRD that La substitution with Sr promoted the segregation of Ni after exsolution at 600 °C and therefore the catalytic activity of the material in comparison to undoped $LaFe_{0.8}Ni_{0.2}O_3$. However, the highest yield of CH_4 was limited to 20% and could only be achieved at high temperature (around 470 °C). Nevertheless, despite few studies dedicated to dry reforming reaction,[37] *in situ* surface-specific characterization of the exsolved perovskite catalysts upon formation of the active phase is missing. *In situ* studies are of particular importance for this system because La-based perovskites are known to be highly reactive towards water/humidity and CO_2, which hinders any attempt for *ex situ*/post mortem surface characterization.

In light of the above aspects, this study explores the use of the stoichiometric $LaNiO_3$ perovskite as a precursor of highly active and stable Ni-supported catalysts towards CO_2 methanation. We used a conventional supported Ni/La_2O_3 material with similar Ni loading as a benchmark catalyst, to demonstrate the superior CO_2 methanation performance of the $LaNiO_3$ exsolved catalyst. We also employed several *ex situ* and *in situ* synchrotron-based characterization techniques to examine the exsolution process and the dynamics of surface evolution of the catalyst during H_2-activation and reaction conditions. The correlation between the surface state and the catalytic performance of exsolved and supported benchmark catalysts offers valuable insights beyond the commonly observed effect of stabilizing Ni nanoparticles. It also provides crucial information regarding surface transformations that govern the reactivity of CO_2 methanation.

2. Experimental part

2.1. Catalyst preparation

2.1.1 Synthesis of $LaNiO_3$ perovskite and reference Ni/La_2O_3 catalysts. The synthesis of $LaNiO_3$ was carried out using

the Pechini sol gel method.[38] A precursor solution was prepared by dissolving an equimolar ratio of metallic salts with two equivalents of citric acid. In particular, $La(NO_3)_3 \cdot 6H_2O$ (11.2 mmol, 4.85 g), $Ni(NO_3)_2 \cdot 6H_2O$ (11.2 mmol, 3.26 g) and citric acid (22.4 mmol, 4.31 g) were dissolved in ethanol (60 mL). Then, the solution was heated at 60 °C for 4 h under continuous stirring until a green gel was obtained. The gel was then dried at 100 °C overnight and crushed into a powder. Finally, the mixture was calcined at 700 °C for 6 h at a heating rate of 2 °C min^{-1} and an intermediate dwell time of 6 h at 500 °C, resulting in a black powder.

The synthesis of Ni/La_2O_3 was realized by wet impregnation. To this end, La_2O_3 was first prepared *via* calcination of $La(NO_3)_3 \cdot 6H_2O$ at 800 °C for 2 h so as to get a surface area comparable to that of the perovskite.[39] Then, $Ni(NO_3)_2 \cdot 6H_2O$ (8.5 mmol, 2.48 g) was added to 1.5 g of La_2O_3 dispersed in 30 mL of distilled water, so as to attain similar Ni/La ratio (Ni/La = 1, 25 wt% Ni) to that in the perovskite based-materials. The mixture was stirred for 4 h at 60 °C. The solvent was then evaporated in a rotary evaporator and dried overnight. For comparison purpose, the powder was then calcined at 700 °C for 6 h using a similar protocol to the one described for the perovskite material and finally treated at 600 °C under H_2 for 30 minutes prior to the catalytic test.

2.1.2 Transformation of the perovskite-based catalysts by reduction pretreatments. The $LaNiO_3$ catalyst was treated under a H_2 atmosphere at selected temperatures to evaluate the CO_2 methanation performance. To this end, a 200 mg sample was loaded in a U-shaped tubular quartz reactor and subsequently reduced at 400, 500 or 600 °C with a heating ramp of 10 °C min^{-1} under 50 mL min^{-1} of H_2 for 30 minutes. Materials after hydrogen treatments were designated with a number indicating the temperature of the treatment, for instance $LaNiO_3$-400, for $LaNiO_3$ treated at 400 °C. These temperatures were specifically chosen to investigate the effects of the gradual transformation of $LaNiO_3$ under a reducing atmosphere on the size and morphology of Ni particles. For all the temperatures studied, the duration of the reduction treatment was intentionally kept relatively short (*i.e.*, 30 minutes) to prevent the nucleation of large Ni particles. As previously demonstrated,[40] temperature has a notable impact on the overall exsolution mechanism, including the density of nuclei, while the treatment duration primarily influences the final step of the process, which is related to the growth of the particles.

2.2. Catalytic evaluation at 1 bar

CO_2 methanation tests were performed in a fixed-bed flow reactor using a U-shaped quartz micro-reactor (i.d. 6 mm). In a typical catalytic test, 100 mg catalyst was diluted with 100 mg SiC, both sieved between 150 and 250 μm and deposited on a quartz wool bed. The quartz reactor was then introduced in a tubular oven with the catalyst bed located in the isothermal zone. The gases were introduced *via* calibrated mass flow controllers (Bronkhorst) for a total flow rate of 20 mL min^{-1} (GHSV = 12 000 h^{-1}). The temperature was controlled by a K-type thermocouple attached to the quartz reactor in intimate contact with the catalytic bed location. Prior to the tests, the samples were first reduced at temperatures ranging between 400 and 600 °C, as already detailed in Section 2.1.2. Then, all catalytic tests were performed at atmospheric pressure in a $CO_2 : H_2$ gas mixture with a 1 : 4 molar ratio. Catalytic runs were performed stepwise starting from 150 to 400 °C using a 10 °C min^{-1} ramp and a dwell time of 30 min at each selected temperature. Long-term stability tests were also conducted at 300 °C for 65 h after H_2 pretreatment at 600 °C. The outlet gas was analyzed using a gas chromatograph Agilent 5975C VL MSD equipped with a Molecular Sieve 5A column, a PoraPLOT U GC column and an OV-1 capillary column and TCD for CO, CH_4, CO_2 and H_2O detection. The detection and quantification of H_2 was not possible due to the similar retention time to that of the carrier gas (He). The formation of CH_4 and CO are due to CO_2 methanation and reverse water-gas shift reactions respectively (eqn (1) and (2)):

$$CO_2 \text{ methanation reaction: } CO_2 + 4H_2 \rightarrow CH_4 + 2H_2O \quad (1)$$

$$\text{Reverse water-gas shift reaction: } CO_2 + H_2 \rightarrow CO + H_2O \quad (2)$$

The CO_2 conversion (X_{CO_2}) and CH_4 selectivity (S_{CH_4}) were calculated as follows:

$$CO_2 \text{ conversion} : X_{CO_2}(\%) = \frac{CO_{2,in} - CO_{2,out}}{CO_{2,in}} \times 100 \quad (3)$$

$$CH_4 \text{ selectivity} : S_{CH_4}(\%) = \frac{CH_{4,out}}{CH_{4,out} + CO_{out}} \times 100 \quad (4)$$

where $CO_{2,out/in}$, $CH_{4,out}$ and CO_{out} are the concentrations at the inlet and outlet of the reactor at each reaction temperature. The concentration of each gas was quantified by the corresponding GC peak areas and the response factor of each gas determined by calibration. Regarding the outlet concentrations, a correction factor based on the carbon balance was integrated into the calculation to take into account the flow variation during the test.

2.3. Characterization techniques

2.3.1 Standard characterization. *Ex situ* X-ray diffraction (XRD) measurements were carried out on a Bruker D8 advance diffractometer equipped with a LynxEye PSD detector using Cu $K\alpha_{1,2}$ radiation ($\lambda = 1.5418$ Å) operating at 40 kV and 40 mA. The XRD patterns were recorded in the 20–85° (2θ) range at a scan rate of 0.032° s^{-1}. Crystallite sizes were estimated according to the Scherrer equation and based on the line broadening of the most intense and isolated reflection (*i.e.*, the (024) reflection at $2\theta = 47.3°$ for $LaNiO_3$ crystallizing in a hexagonal system and the (111) reflection at $2\theta = 44.8°$ for fcc Ni).

N_2 physisorption measurements were performed on a Micromeritics Tristar 3000 apparatus. The surface area was determined by a multiple-point Brunauer–Emmett–Teller (BET) approach with relative pressures (p/p_0) ranging between 0.05 and 0.35. Prior to the adsorption–desorption of N_2 realized at −196 °C, 100 mg sample was first degassed at 200 °C under primary vacuum for a minimum of 6 h.

H_2 Temperature Programmed Reduction (H_2-TPR) experiments were carried out using a Micromeritics Autochem 2920 device equipped with a thermal conductivity detector (TCD). The profiles were obtained after loading 100 mg of sample in a U-shaped quartz reactor and reduction under 10% H_2 in Ar with a flow rate of 20 mL min^{-1} up to 900 °C, with a heating rate of 10 °C min^{-1}. A cold trap was installed at the outlet of the reactor to remove the moisture produced during reduction.

Transmission Electron Microscopy (TEM) was performed using an FEI Talos F200X microscope operating at 200 kV in scanning transmission electron microscopy (STEM) mode using high-angle annular dark-field (HAADF) imaging. Energy-dispersive X-ray spectroscopy (EDX) using a Super-X system with four silicon drift detectors (SDDs) was applied to the detection of differences in local chemical composition.

2.3.2 Ambient pressure photoemission characterization. Synchrotron-based photoemission experiments (Ambient-Pressure X-ray Photoelectron Spectroscopy, (AP-XPS) and Ambient-Pressure Hard X-ray Photoemission Spectroscopy (AP-HAXPES)) were performed during 3 separate beamtimes in two different instruments. Both apparatuses were equipped with the same electron energy analyser (Phoibos 150NAP by SPECS™) which operated at the same pass energy, while the same soft X-ray excitation photon energies were used for recording. Unless otherwise stated the photon energy was selected so as to provide photoelectrons with two kinetic energies (200 and 460 eV) for each of the core level of the elements analyzed (O 1s, C 1s, La 3d and Ni 2p). The information depth is estimated as 3 times the photoelectron inelastic mean free path retrieved from ref. 41. Quantification of the elements was performed after normalization of the intensities by taking into account the photon flux and the atomic subshell photoionization cross-sections using the SESSA (Simulation of Electron Spectra for Surface Analysis) software.[41] The binding energy (BE) of the core level peaks was referenced to the Fermi level cut-off defined in a separate measurement of the Ni 3d states of metallic nickel ("0" in the BE scale),[42] assuming that the Fermi edge of the samples is in electrical contact with the spectrometer. This procedure was repeated for each photoelectron peak and found to give a BE for the C 1s of hydrocarbon species at 284.7 ± 0.1 eV. Unless otherwise stated, the error in the reported BEs is ±0.1 eV. The XPS spectra were analyzed using CasaXPS software.

In all cases, 20 mg of catalyst was pelletized and fixed on the sample holder, while a 1 : 1 CO_2 : H_2 mixture was employed. It is important to note that, according to the balanced chemical equation for the Sabatier reaction, a CO_2 : H_2 molar ratio of 1 : 4 is required, and this ratio was indeed used in the 1 bar catalytic tests. However, under the specific low-pressure conditions of the *in situ* AP-XPS experiments, this ratio might not be optimal for the reaction. In this context, we investigated the effect of the CO_2 to H_2 ratio at 5 mbar overall pressure and temperatures between 200 and 300 °C, in a reactor attached to a laboratory XPS setup described previously.[43] According to the online gas phase analysis, a CO_2 : H_2 ratio of 1 : 1 resulted in about 25% higher CH_4 and H_2O signals compared to 1 : 4. This increase could be attributed to an extended contact time between CO_2 and the catalyst. Therefore, selecting a CO_2 : H_2 ratio of 1 : 1 is a good compromise to maximize CH_4 production in the low-pressure range under AP-XPS testing conditions. Below follows a description of the two AP-XPS instruments used in this study.

2.3.2.1 AP-XPS at the tempo beamline. The AP-XPS instrument of Sorbonne University attached to the TEMPO beamline of the SOLEIL Synchrotron radiation facility (France)[44] was used to characterize the $LaNiO_3$ catalyst under O_2, H_2 (sample treated at 600 °C) and CO_2 : H_2 (1 : 1) methanation reaction conditions. The gas feeds (O_2, H_2, CO_2) were regulated by leak valves and their purity was monitored using a quadrupole mass spectrometer. The catalyst was fixed on a sample holder with an integrated resistive heater and the temperature was monitored by a K-type thermocouple in contact with the sample surface.

2.3.2.2 AP-XPS and AP-HAXPES at the EMIL beamline. Combined AP-XPS and AP-HAXPES measurements were performed at the new CAT branch of the EMIL beamline at the synchrotron radiation facility BESSY II of the Helmholtz Zentrum Berlin.[45,46] The reported measurements of $LaNiO_3$ catalyst in H_2 (sample treated at 400 °C) as well as of the supported Ni/La_2O_3 catalyst under H_2 (sample treated at 600 °C) and CO_2 : H_2 (1 : 1) methanation reaction conditions were performed using this instrument. The catalyst was mounted on a sample stage heated from the rear with an IR laser irradiating the plate placed under the pellet. Gases (H_2, O_2, CO_2) were introduced into the sample chamber *via* calibrated mass flow controllers (Bronkhorst). The gas phase composition was monitored using a differentially pumped quadrupole mass spectrometer (QMS, Pfeiffer PrismaPro) connected to the sample chamber through a leak valve. A significant feature of the CAT@EMIL beamline is the possibility to use soft and tender X-ray radiation in one single experiment, allowing depth profiling from the extreme surface to the subsurface. The AP-XPS spectra were measured with a 60 μm exit slit, while for AP-HAXPES a double crystal monochromator (DCM) that works without an exit slit was used. In the AP-HAXPES two fixed photon energies were used ($h\nu$ = 3005 and 4900 eV) (maximum analysis depth around 21 nm).

2.3.3 X-ray absorption fine structure. All the presented Ni K-edge X-ray Absorption Fine Structure (XAFS) spectra were measured at the BM23 beamline[47] of the European Synchrotron Radiation Facility. The monochromatic beam was obtained with the Double Crystal Monochromator and harmonics were rejected by a Si(111) double mirror. Spectra were collected in transmission mode using three ion chambers (30 cm) filled with 1.248 mbar of N_2 (I_0) or 0.271 mbar of Ar (I_1/I_2) and topped up to 2 bar with He. The sample, in the form of 13 mm^2 pellet diluted in BN, was located between the first (I_0) and the second (I_1) ion chambers while Ni metal foil (for energy calibration and alignment) was placed between I_1 and the last chamber (I_2). For *ex situ* spectra the sample was held in a conventional sample holder while *in situ* measurements were performed by placing the sample in a Microtomo cell.[48] The *in situ* experiment was performed by flowing 50 mL min^{-1} of 20% H_2 : He gas mixture during the temperature ramp protocol reported in Fig. S1.† X-ray Absorption Near Edge Structure (XANES) spectra reported in Fig. 5a in the text concern the regions of the protocol indicated with a red line while the magnitude component of FT-

EXAFS spectra reported in Fig. 5d and S9† was collected during steady states indicated by the triangle. Spectra of *ex situ* samples and steady states of *in situ* experiment were collected with the step scan mode in the 8.19–9.31 keV energy range. A constant acquisition time of 0.5 s per point was employed throughout the measured energy range. Energy resolution was set to 5 eV per point for the pre-edge (8.19–8.3 keV) and 0.3 eV per point for the XANES (8.31–8.34 keV) while a constant *k*-spacing of 0.035 k per point was used in the EXAFS region (8.34–9.31 keV). Spectra collected during heating/cooling steps of the *in situ* experiment were measured in continuous mode in the 8.2–9.2 keV energy range with 0.3 eV per point energy resolution and 0.05 s per point time resolution for a total of 3 minutes per scan. Energy calibration and alignment together with background subtraction and edge jump normalization were conducted with a dedicated Python script based on the Larch library.[49] Linear Combination Analysis was done using Larch-based Python scripts. The weight of the single component (w_i) was constrained to be $0 < w_i < 1$ while the sum of the component weights $\left(\sum_i w_i\right)$ was not forced to 1. The closeness of $\sum_i w_i$ to 1 was used as an additional qualitative indicator of the goodness of the fit. All the presented FT-EXAFS spectra were obtained using a Hanning window in the 2.5–13.3 $Å^{-1}$ *k*-range. The *k*-range of FT-EXAFS extraction and *R*-range of FT-EXAFS fit are reported in Table S1.† FT-EXAFS fit was conducted using the Artemis software from the Demeter package.[50] The passive amplitude reduction factor S_0^2 was evaluated from the fit of reference Ni^0 spectra (see Fig. S9 and Table S1†) and fixed for the fit of the other spectra. EXAFS Wavelet Transform (WT) was calculated with the Cauchy wavelet function fixing η to 6.4.[51]

3. Results

3.1. CO_2 methanation performance

Fig. 1a displays the CO_2 conversion (X_{CO_2}) and CH_4 selectivity (S_{CH_4}) profiles of the methanation light-off tests over perovskite $LaNiO_3$ catalyst activated by reduction in H_2 at 400, 500 and 600 °C, hereafter abbreviated as $LaNiO_3$-400, $LaNiO_3$-500, $LaNiO_3$-600. The X_{CO_2} and S_{CH_4} curves of supported Ni/La_2O_3 pre-reduced at 600 °C are included for comparison. The X_{CO_2} increases rapidly above 200 °C, while at 400 °C it attains CO_2 conversion values close to thermodynamic equilibrium indicated by the dashed-brown line in Fig. 1a. The CO_2 conversion curves of $LaNiO_3$ are shifted towards lower temperatures compared to Ni/La_2O_3. The shift becomes more pronounced as the activation temperature of $LaNiO_3$ increases from 400 °C to 600 °C, indicating improvement of the catalytic activity with the increase of the activation temperature. This can be quantified by the light-off temperatures corresponding to 50% conversion (T_{50}) determined from Fig. 1a and listed in Table 1. It is evident that in the case of $LaNiO_3$ the T_{50} shifts up to 100 °C compared to Ni/La_2O_3, which represents an enormous difference in the catalytic performance. Note that the X_{CO_2} and S_{CH_4} of Ni/La_2O_3 is comparable to those of similar La_2O_3 supported Ni catalysts.[25] In addition, the $LaNiO_3$ is more selective than Ni/La_2O_3 in the production of CH_4 (top part of Fig. 1a), while S_{CH_4} further improves with H_2-activation temperature. For example, S_{CH_4} of $LaNiO_3$-600 remains above 97% throughout the experiment and reaches 99.7% at 350 °C while that of Ni/La_2O_3 rests around 92%. The apparent activation energies (E_{app}) determined from Arrhenius plots (Fig. S2†) are listed in Table 1. In all cases the E_{app} is between 87 and 99 kJ mol^{-1}, which is in the range typically reported for CO_2 methanation over Ni-based catalysts.[52]

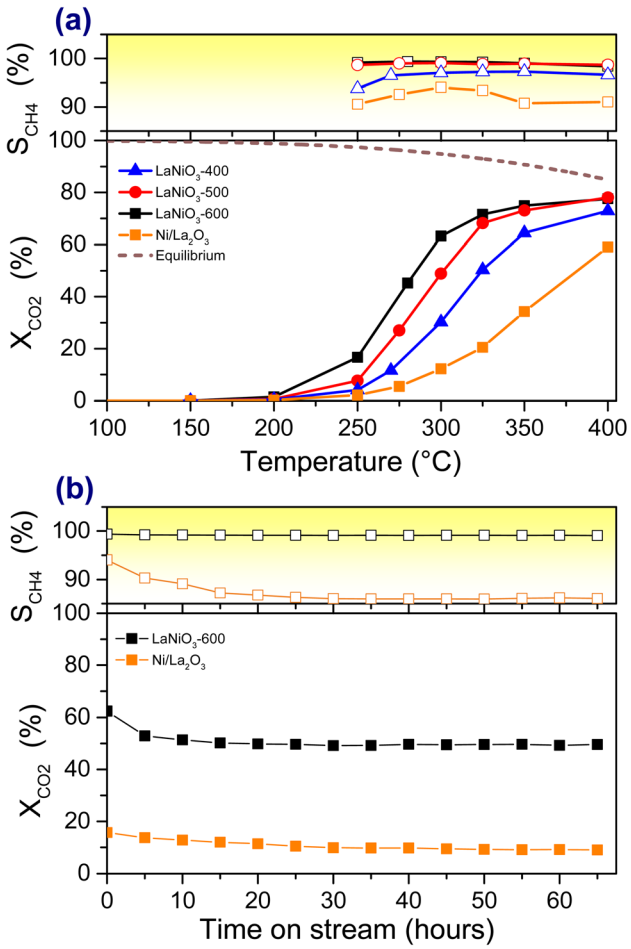

Fig. 1 CO_2 methanation performance of $LaNiO_3$ and Ni/La_2O_3 catalysts: (a) CO_2 conversion and CH_4 selectivity as a function of the reaction temperature. The thermodynamic limit of CO_2 conversion is included as a dashed-line. (b) Long-term stability tests at 300 °C for catalysts pre-reduced at 600 °C. All catalytic tests were performed in 20% CO_2/H_2 at 1 bar (100 mg mixed in 100 mg of SiC, GHSV ~12 000 h^{-1}).

Table 1 The light-off temperatures corresponding to 50% conversion (T_{50}) determined from Fig. 1a and the apparent activation energies (E_{app}) determined from Arrhenius plots (Fig. S1)

Catalyst	T_{50} °C	E_{app} kJ mol^{-1}
$LaNiO_3$-400	325	99
$LaNiO_3$-500	300	96
$LaNiO_3$-600	285	87
Ni/La_2O_3	381	93

The durability tests of $LaNiO_3$-600 and Ni/La_2O_3 catalysts (Fig. 1b) reveal that the perovskite catalyst is not only more active and selective, but also far more stable than the supported one. In particular, after a decrease in the relative CO_2 conversion of about 20% observed within the first 10 h, $LaNiO_3$ does not present any sign of further deactivation up to 65 h. In addition, throughout these tests, the CH_4 selectivity remains always above 99%. This performance clearly outperforms that of the Ni/La_2O_3 catalyst, which has lower CO_2 conversion and CH_4 selectivity also being less stable.

Overall, the catalytic tests show that the $LaNiO_3$ perovskite catalyst outperforms the conventional supported Ni/La_2O_3, while higher H_2 activation temperatures seem to promote both CO_2 conversion and CH_4 selectivity of $LaNiO_3$.

3.2. *Ex situ* structural and morphological characterization

3.2.1 XRD, H_2-TPR and N_2-BET. The XRD patterns (Fig. 2a) of the fresh calcined $LaNiO_3$ is characteristic of the monophasic hexagonal perovskite structure (JCPDS no. 34-1181) without any evident NiO, La_2NiO_4 or La_2O_3 impurities. The diffraction peaks of hexagonal $LaNiO_3$ are still visible after H_2-activation at 400 °C ($LaNiO_3$-400), but vanish at 500 and 600 °C. Instead, new Bragg reflections appeared due to metallic nickel (Ni^0) and h-La_2O_3 phases (see Table 2). The Ni^0 crystallite size calculated by XRD (Table 2) is about 4 nm at 400 °C and increases to 6 nm at 600 °C. The XRD pattern of the spent catalyst, after the methanation reaction ($LaNiO_3$-sp), is clearly modified as compared to that of the prior H_2-activated state. A new hexagonal lanthanum oxycarbonate phase (II-$La_2O_2CO_3$, JCPDS 37-0804) was found,[53,54] together with the h-La_2O_3 and metallic Ni phases already existing on the reduced sample. The diffractogram of reduced Ni/La_2O_3 is dominated by the diffraction lines of Ni^0 and h-La_2O_3 phases and remains identical after the methanation reaction (Fig. 2b).

The H_2-TPR profile of $LaNiO_3$ calcined at 700 °C (Fig. 2c) is dominated by two main and several smaller H_2 consumption peaks. This shows that the reduction of $LaNiO_3$ occurs in two steps at approximately 400 and 550 °C. The H_2 consumption ratio between the two main reduction peaks is about 1.5. The H_2-TPR profile of Fig. 2c is in fair agreement with previous reports.[37,55,56] Usually, the low temperature peak is attributed to the $Ni^{3+} \rightarrow Ni^{2+}$ reduction and the one at higher temperature to $Ni^{2+} \rightarrow Ni^0$.[37] Although formation of Ni^0 in the second reduction step is related to the transformation of the perovskite to La_2O_3, both $La_2Ni_2O_5$ (ref. 37) and La_2NiO_4 (ref. 57 and 58) have been proposed as the intermediate lanthanum phase of the first reduction step. The *in situ* XANES spectra (see *infra*) provide more insight on $LaNiO_3$ reduction. The profile of Ni/La_2O_3 shows two main peaks around 400 and 500 °C. According to previous reports[59] the one at 400 °C is due to the reduction of Ni^{2+} species with possible contribution of Ni^{3+}. The smaller peak around 500 °C has been ascribed to the reduction of Ni–La_2O_3 solid solution probably formed during calcination at the interface of the two elements.

The specific surface areas deduced from N_2 physisorption measurements are included in Table 2. The surface area of the calcined catalyst is low and, as might be expected, decreases more with the increase of the reduction temperature and remains below the detection limit of conventional N_2-BET

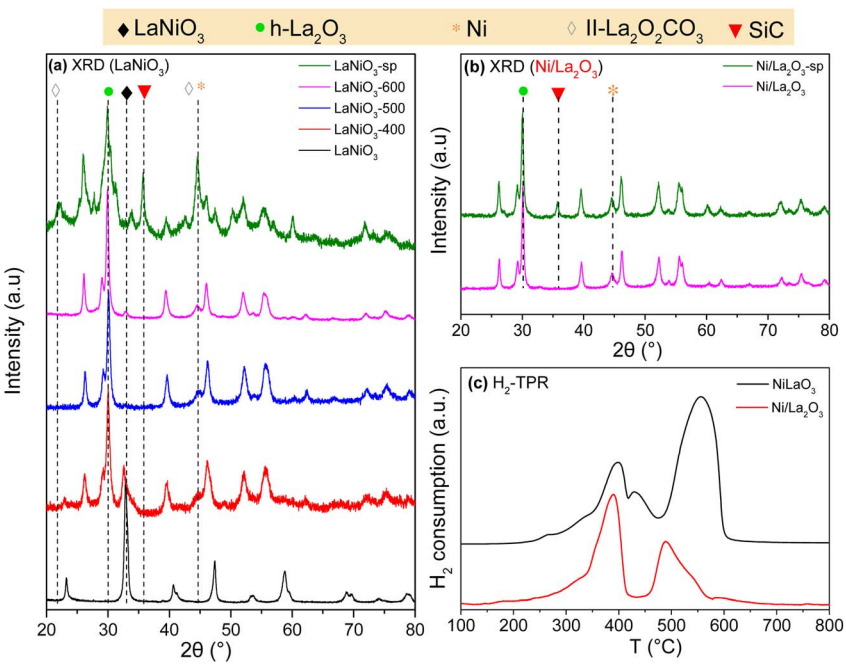

Fig. 2 XRD patterns of (a) $LaNiO_3$ catalysts measured after calcination, H_2-activation at 400, 500 and 600 °C ($LaNiO_3$-400, $LaNiO_3$-500 and $LaNiO_3$-600) and after long-term stability methanation test ($LaNiO_3$-sp), (b) Ni/La_2O_3 catalysts measured after H_2-activation at 600 °C (Ni/La_2O_3) and after long-term stability methanation test (Ni/La_2O_3-sp). The SiC-related peaks appear in the diffractograms of the spent catalysts, (c) H_2-TPR profile of $LaNiO_3$ and Ni/La_2O_3 catalysts.

Table 2 Physico-structural properties of calcined, H_2-activated and spent $LaNiO_3$ and Ni/La_2O_3 catalysts

Sample	S_{BET} ($m^2.g^{-1}$)	D_{Ni}[a] (nm)	La-based crystalline phases detected	D_{LaOx}[a] (nm)	d_{Ni}[b] (nm)
$LaNiO_3$	3	—	$LaNiO_3$	—	—
$LaNiO_3$-400	2	6	$LaNiO_3$, h-La_2O_3	12.9 (h-La_2O_3)	4.2 ± 0.5
$LaNiO_3$-500	<1	8	h-La_2O_3	14.5 (h-La_2O_3)	N/A
$LaNiO_3$-600	<1	8	h-La_2O_3	17.5 (h-La_2O_3)	6.4 ± 0.2
$LaNiO_3$-sp	N/A	N/A	h-$La_2O_2CO_3$, h-La_2O_3	17.3 (h-La_2O_3)	6.4 ± 0.2
Ni/La_2O_3-600	<1	11	h-La_2O_3	18.9 (h-La_2O_3)	N/A
Ni/La_2O_3-sp	N/A	11	h-La_2O_3	19.5 (h-La_2O_3)	N/A

[a] Average crystallite size estimated by XRD using the Scherrer equation. [b] Average particle size determined by TEM.

measurements. Nevertheless, the surface areas of the perovskite and supported catalyst after reduction are similar, which essentially rules out the possibility that the observed differences in the reactivity are related to the surface area of the catalysts.

3.2.2 HR-TEM and TEM/EDX mapping. The morphology of activated and spent $LaNiO_3$ catalysts is examined by High Resolution Transmission Electron Microscopy HR-TEM combined with Energy Dispersive X-ray elemental mapping (TEM-EDX). Fig. 3 shows representative images of perovskite catalysts after reduction at 400 and 600 °C, as well as those of the spent catalyst. Lower magnification TEM and TEM-EDX images can be found in Fig. S3.† The HR-TEM images display rounded dark-contrast particles within a lighter matrix. The corresponding EDX mapping reveals that these features correspond to Ni-rich particles laid into a lanthanum oxide matrix, evidencing the Ni exsolution during the H_2-activation treatment. In several cases the Ni particles seem to be cast into lanthanum rather than being simply supported on it. A closer look at the TEM and EDX mapping images indicates that in the case of $LaNiO_3$-400 some particles are covered by a nanometer thick layer containing lanthanum. This can be better observed in the La map of this sample (indicated by an arrow), where La looks to have a ring-type, instead of socket-type, morphology. In addition, in some areas of $LaNiO_3$-400 the distribution of Ni and La signals seems quite homogeneous basically revealing mixed Ni–La perovskite areas. This is a sign of a transient state where Ni particles start to nucleate but not yet completely exsolved on the surface, in accordance with the XRD results of Fig. 2a.

The La overlayer and the mixed Ni–La areas disappear in $LaNiO_3$-600 but the Ni particles still look cast into lanthanum (see areas marked with arrows). This morphology resembles the classical exsolution process involving socking of metal nanoparticles into the support.[60] The HR-TEM and TEM/EDX images after the long-term stability tests ($LaNiO_3$-sp) show that the morphology generated during the activation process, comprising homogeneously distributed nano-sized Ni particles, is largely preserved. In addition, there is no evidence of filamentous carbon deposition after the reaction.

The Ni particle size distribution is included in the form of histograms at the bottom of Fig. 3. It is estimated by measuring the size of at least 120 Ni particles identified in the TEM images. Accordingly, the average Ni particle size increases slightly from around 4 to 6 nm when the reduction temperature rises from 400 to 600 °C, in fair agreement with the crystallite sizes estimated from XRD measurements (Table 2). The histograms of the spent catalyst show that the long-term reaction does not affect the Ni particle size and distribution. The stability of highly dispersed metal nanoparticles formed through exsolution from the perovskite matrix is consistent with previous reports.[26] What is of particular interest here is that XRD and TEM results confirm that there is practically no sintering of Ni particles even after 65 hours under the reaction conditions which is a key feature that explains the long-term stability found in Fig. 1b.

3.2.3 *Ex situ* XANES analysis. *Ex situ* Ni K-edge XANES measurements of $LaNiO_3$ and Ni/La_2O_3 catalysts, together with the spectra of reference compounds are shown in Fig. 4a. The XANES measurements confirm the formation of metallic Ni after H_2-activation and catalytic tests, as explained in detail in the ESI.† In order to quantify the various Ni phases, Linear Combination Analysis (LCA) was conducted on the Ni K-edge using reference spectra from NiO, Ni, $LaNiO_4$ and $LaNiO_3$ samples (see Fig. S6†). The LCA results (Fig. 4b) suggest that $LaNiO_3$ is the dominant phase in the fresh perovskite catalyst (≈84%) with minor contribution of La_2NiO_4 (≈12%) and NiO (2%) phases. Notably, the $LaNiO_3$-phase does not resist the H_2 activation process, in contrast to the La_2NiO_4-phase which is maintained in H_2 but disappears after the reaction. This indicates that the transformation of $LaNiO_3$ catalyst does not conclude during H_2-activation, but it still continues under the reaction conditions. Apart from the expected metallic Ni^0, LCA also suggests a considerable amount of NiO-phase which decreases gradually going from the activated to spent $LaNiO_3$ catalysts. A similar trend in the NiO-phase evolution is also observed in the case of Ni/La_2O_3. At this stage it is not clear if NiO formation is part of the $LaNiO_3$ reduction mechanism as proposed earlier,[60] or it is the consequence of Ni^0 oxidation due to air exposure (*ex situ* measurements). More details about the reduction mechanism will be provided by the *in situ* XAFS measurements in H_2 (*vide infra*).

Aiming to confirm LCA results and to eventually estimate NiO and Ni^0 particle dimensions, FT-EXAFS spectra were fitted considering the components evaluated by the LCA procedure (Fig. S7a and b†). The results (Table S1†) show that for both $LaNiO_3$ and Ni/La_2O_3 catalysts metallic and oxidized Ni particles possess bulk-like coordination numbers (CNs) obtained for average particle dimension larger than 3 nm. This finding is

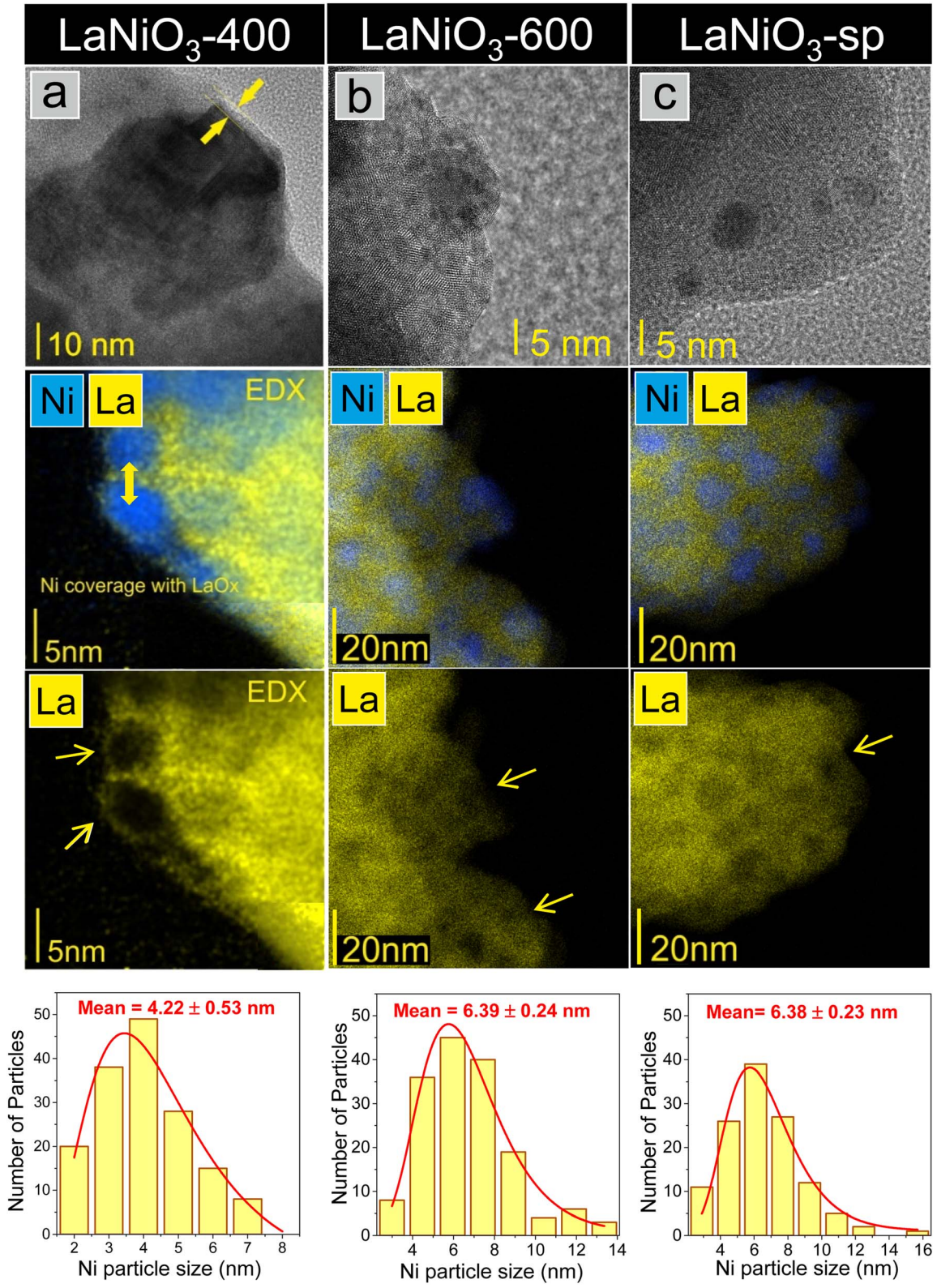

Fig. 3 HR-TEM and TEM/EDX elemental mapping images of (a) $LaNiO_3$-400, (b) $LaNiO_3$-600, and (c) $LaNiO_3$-sp catalysts. The Ni particle-size distribution histogram for each catalyst is included at the bottom of the figure. Between 120 and 200 particles were analyzed depending on the sample. Isolated O, Ni and La elemental mapping of the selected regions are depicted in Fig. S4.†

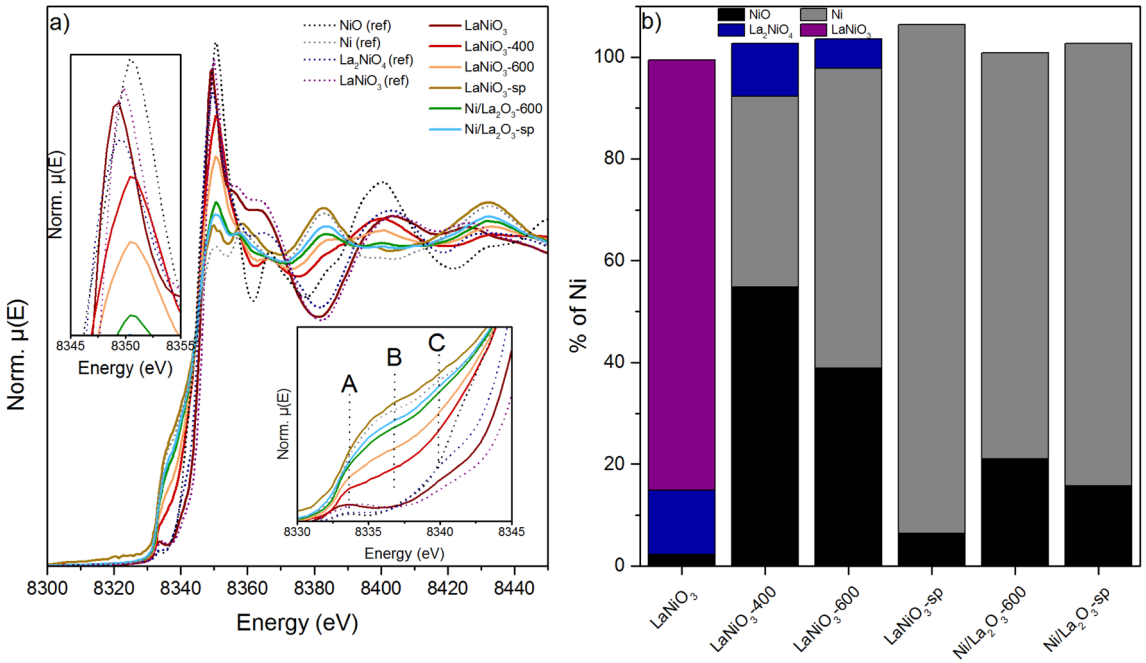

Fig. 4 (a) *Ex situ* Ni K-edge XANES spectra collected on $LaNiO_3$ and Ni/La_2O_3 catalysts and reference materials. Details of pre-edge transitions is reported in the inset. (b) Results of LCA analysis conducted on the Ni K-edge of $LaNiO_3$ and Ni/La_2O_3. The experimental spectra and the best fit curves are reported in Fig. S6.†

complementary to the TEM/EDX analysis since particles smaller than 3 nm fall within the detection limit of the TEM/EDX.

3.3. *In situ* spectroscopy of $LaNiO_3$ during H_2-activation treatment

The results of Fig. 1 showed a critical effect of the H_2-activation temperature on the catalytic performance, while *ex situ* analysis reveals major transformations of the perovskite catalyst after the activation and methanation reaction. For a better assessment, the fresh $LaNiO_3$ catalyst was studied during H_2-activation by *in situ* XAFS and AP-XPS. Hard, tender and soft X-rays were employed in these measurements providing complementary information in a broad analysis depth range.

3.3.1 *In situ* XANES analysis in 1 bar 20% H_2/He flow. X-ray absorption spectra of $LaNiO_3$ were collected at 1 bar 20% H_2/He both during stepwise temperature ramping (10 °C min^{-1}) and consequent steady state measurements at 100 °C (see Fig. S1†). The evolution of Ni K-edge with temperature is shown in Fig. 5a, while steady state spectra after annealing at 400 °C, 500 °C and 600 °C, together with spectra of reference samples are compared in Fig. 5b. The evolution of Ni K-edge (Fig. 5a) between 250 °C and 500 °C shows a gradual decrease of the white-line peak intensity with parallel increase at the rising edge, while above 500 °C the Ni K-edge remains practically stable. Comparison of steady state EXAFS spectra with reference curves (Fig. 5b) indicate that the calcined catalyst contains mainly the $LaNiO_3$-phase, while this phase is fully transformed into Ni^0 upon annealing in H_2 at 500 °C, in line with the *ex situ* XANES measurements discussed above. The FT-EXAFS (Fig. 5c) supports the drastic changes of Ni local structure during reduction treatment. Comparison of the relative intensity of the Ni–Ni (metal) path of $LaNiO_3$-500 and $LaNiO_3$-600 with that of the Ni^0 reference suggests that Ni–Ni CN is lower than the bulk value (CN = 12) implying that Ni metal particles are smaller than 3 nm.[61,62]

LCA of the Ni K-edge by four reference line shapes was performed to quantify the evolution of the different Ni phases during $LaNiO_3$ reduction. As displayed in Fig. 5d the fresh/calcined catalyst is a mixture of 82% $LaNiO_3$, 12% La_2NiO_4 phases and 3% NiO. At 400 °C the $LaNiO_3$ phase is converted to 33% Ni^0–66% La_2NiO_4 mixture following reaction (1). Above this temperature La_2NiO_4 reduces fast to Ni^0, most likely leading to the production of La_2O_3 by reaction (2). At 500 °C the $LaNiO_3$ reduction is completed and at higher temperatures, the Ni K-edge shows no further changes.

$$2LaNiO_3 + 2H_2 \rightarrow La_2NiO_4 + Ni + 2H_2O\ (100\text{–}400\ ^\circ C) \quad (1)$$

$$La_2NiO_4 + H_2 \rightarrow Ni + La_2O_3 + H_2O\ (400\text{–}500\ ^\circ C) \quad (2)$$

The gradual decomposition of $LaNiO_3$ into La_2NiO_4 and presumably to La_2O_3 in the final reduction step, along with the appearance of metallic Ni deduced by our XAFS results agrees with the findings of a recent TEM and XRD study of $LaNiO_3$ treated under vacuum and inner gas (*i.e.* He).[60] However, in our case the addition of H_2 changes the process suggested in ref. 60 in two ways. The first is related to the NiO formation clearly evident under inert or vacuum conditions due to oxygen diffusion from the perovskite lattice towards exsolved Ni. In our case, NiO does not appear in the absorption spectra because, if it forms, it is quickly reduced by gas phase H_2 to Ni^0. The second

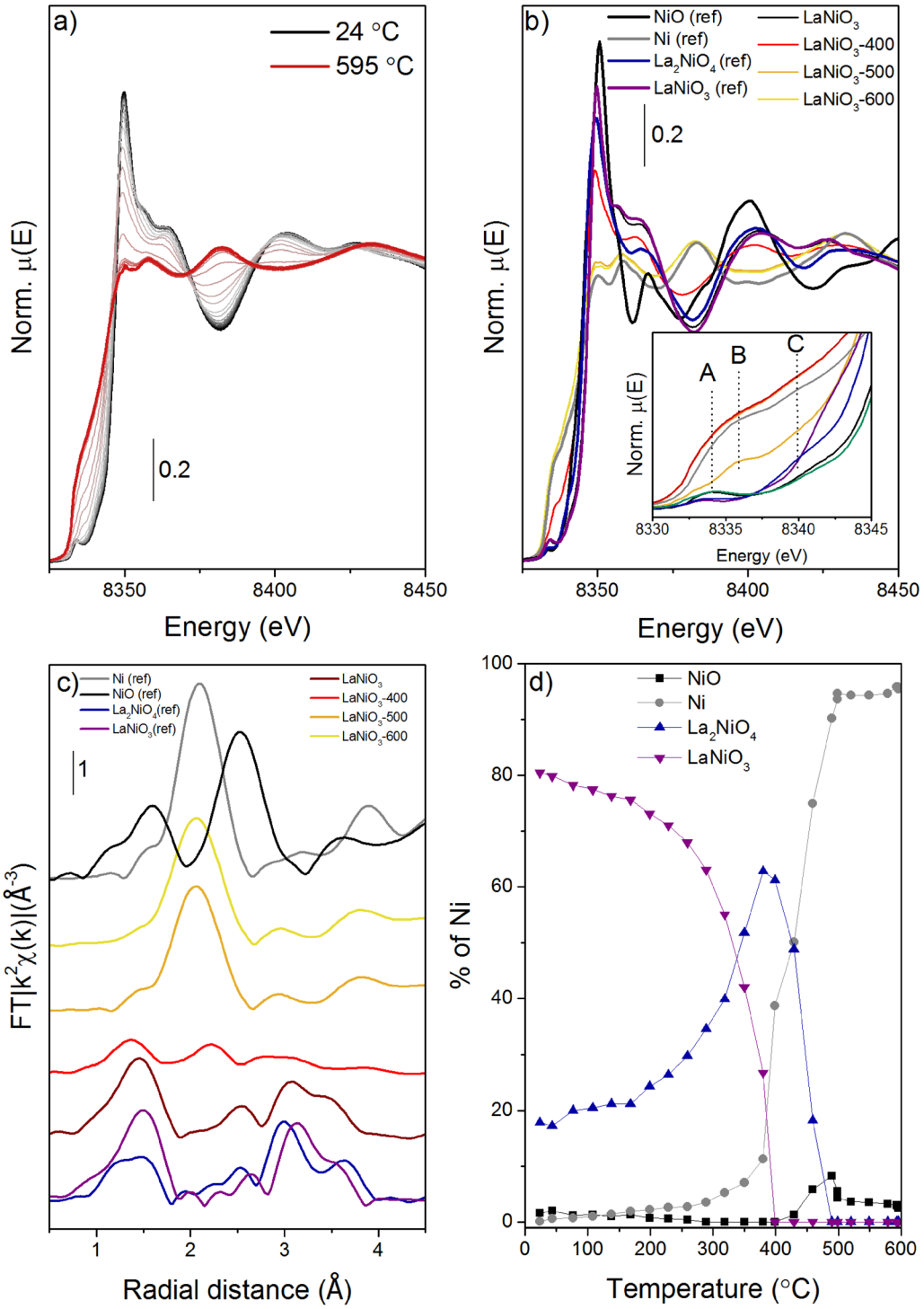

Fig. 5 (a) Ni K edge evolution from RT to 600 °C, (b) separate graph of references and spectra recorded under steady state conditions, (c) magnitude component of phase uncorrected FT-EXAFS and (d) phase evolution as a function of temperature according to LCF. Experimental EXAFS spectra together with LCA results on the whole thermal treatment and LCA best/worst fit are reported in Fig. S10.†

difference is the temperature of the perovskite transformation. We found that the $LaNiO_3$-phase in H_2 decomposes between 200 and 500 °C, while under an inert atmosphere this window shifts to considerably higher temperatures (*ca.* 550–800 °C). Interestingly, a small quantity of NiO was observed above 500 °C which would imply La_2NiO_4 decomposition to La_2O_3 and NiO. Since at T > 500 °C under H_2 the latter should be directly reduced to Ni, this spectral feature should be more reasonably ascribed to a not fully reduced Ni-oxidic phase.

Finally, comparison of the Ni K-edge LCA results between *ex situ* (Fig. 4b) and *in situ* (Fig. 5d) treated $LaNiO_3$ catalyst shows many similarities but also some differences. In particular, both

set of measurements agree on the decomposition of the $LaNiO_3$-phase to La_2NiO_4 up to 400 °C and its full conversion to Ni^0 at 600 °C. However, *in situ* measurements show relatively more La_2NiO_4 at 400 °C and considerably less NiO as compared to the *ex situ* results. In addition, *ex situ* FT-EXAFS analysis suggested Ni clusters with a bulk-like electronic structure while *in situ* results anticipated the CN to be lower than the bulk value. These differences can be rationalized by the milder reduction conditions applied in the *in situ* XAFS measurements (diluted H_2 in the Microtomo cell instead of pure H_2 in the quartz tube for the *ex situ* treatment). It is therefore possible that *in situ* spectra depict the formation of atomically dispersed Ni at the early stages of the exsolution process, before their agglomeration into nanoparticles with a bulk-like electronic structure shown in the *ex situ* results. Besides, the small amount of NiO during *in situ* measurements suggests that the NiO observed during *ex situ* analysis was the result of sample oxidation in air. Based on that, one can also speculate that the reason behind the differences in the relative NiO amount among the catalysts shown in Fig. 4b is due to differences in Ni particle size. The NiO upon exposure in air forms a passivation layer around Ni^0 particles. The bigger the particles the lower the NiO contribution in the Ni K-edge (bulk sensitive method) since they have a lower surface to volume ratio. If this assumption is valid, one can conclude that LCA results of Fig. 4b indirectly show that the Ni particle size on our perovskite catalyst is in the order $LaNiO_3$-400 < $LaNiO_3$-600 < $LaNiO_3$-sp. In addition, the size of Ni particles for Ni/La_2O_3 catalysts is in similar order to that of $LaNiO_3$ after reduction, but probably becomes much bigger after the reaction.

3.3.2 X-ray photoemission spectroscopy. The adjustment of $LaNiO_3$ surface upon H_2 activation was followed *in situ* by synchrotron-based AP-XPS/HAXPES. Fig. 6a presents the La 3d and Ni 2p spectra of the fresh/calcined catalysts initially collected in 2 mbar O_2 and consequently in H_2 at 400 and 600 °C. The shape of the La 3d and Ni 2p curves is complex due to Ni

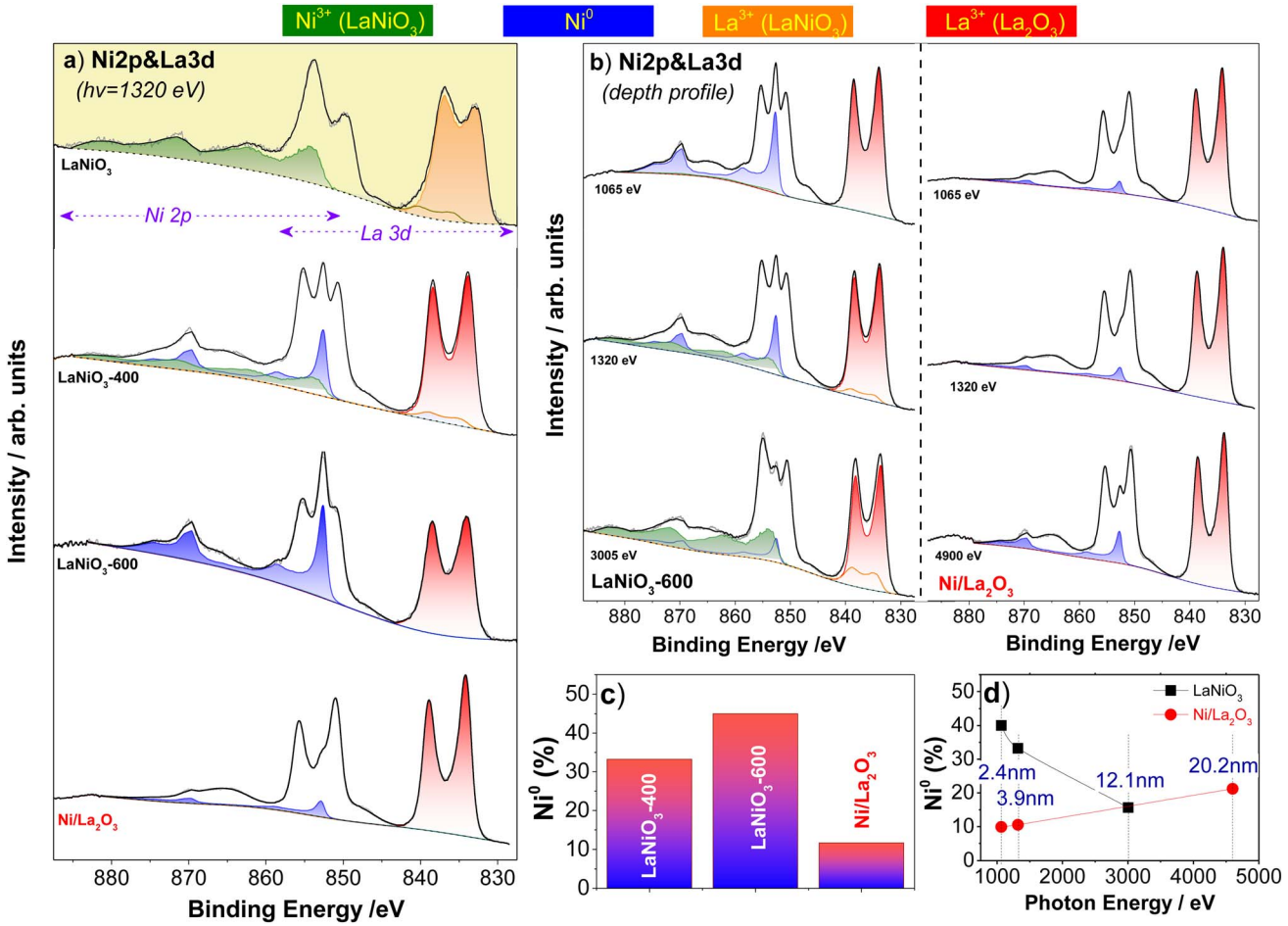

Fig. 6 (a) *In situ* La 3d and Ni 2p AP-XPS spectra of the fresh/oxidized $LaNiO_3$ catalyst (2 mbar O_2 at 400 °C), H_2-activated catalyst (2 mbar H_2 at 400 °C and 600 °C) and Ni/La_2O_3 catalyst (2 mbar H_2 at 600 °C), (b) depth-dependent La 3d and Ni 2p spectra of $LaNiO_3$-600 (left panel) Ni/La_2O_3 catalysts (left panel) measured at 400 °C in 2 mbar H_2 at three different photon energies. For the La 3d & Ni 2p curve fitting peak line-shapes derived from reference materials and synthetic line-shapes derived by a mathematical formula were used. For clarity only the La $3d_{5/2}$ and Ni 2p fitting components are shown. (c) Bar graph showing the $\%Ni^0$ atomic concentration of different samples calculated by the Ni 2p and La 3d peak areas (spectra measured at 400 °C in 2 mbar H_2 with photons of $h\nu = 1320$ eV giving an estimated analysis depth of approx. 3.9 nm). (d) The evolution of $\%Ni^0$ as a function of the excitation energy for the two catalysts measured at 400 °C in 2 mbar H_2. The information depth in each photon energy is estimated as 3 times the photoelectron inelastic mean free path.

$2p_{3/2}$ and La $3d_{3/2}$ peak overlap and the presence of multiple satellite and plasmon loss features associated with the different oxidation states of Ni and La.[63] Nevertheless, the contribution of Ni^0 in the spectrum can be identified by the sharp Ni $2p_{3/2}$ feature at 852.6 eV. As displayed in Fig. 6a, this feature is absent in the calcined catalyst, but appears in the $LaNiO_3$-400 spectrum and is further amplified for $LaNiO_3$-600, suggesting that Ni^0 concentration is enhanced at higher reduction temperatures. Clear modifications between oxidizing and reducing conditions are also observed in the La $3d_{5/2}$ doublet around 837 eV. These modifications are consistent with the expected transformation of $LaNiO_3$ into Ni^0 + La_2O_3 upon reduction indicated in the *in situ* XAFS measurements.

To quantify the evident differences in the curve shape, the Ni 2p and La 3d spectra in Fig. 6a were fitted by a linear combination of synthetic peaks and spectra of reference compounds (details are presented in Fig. S11†). The spectrum of the reduced Ni/La_2O_3 catalyst was fitted using the same approach and is included at the bottom of Fig. 6 for comparison. The curve fitting reveals the coexistence of 2 Ni and 2 La components. In particular, ionic Ni (likely Ni^{3+} of $LaNiO_3$) dominates the calcined sample and upon H_2 annealing it is gradually replaced by Ni^0. Likewise, La from the perovskite lattice (La^{3+} of $LaNiO_3$) is stepwise transformed into La^{3+} of La_2O_3 (*vide infra*). The %Ni, determined by the La 3d and Ni 2p areas (Fig. 6c), reveals a net enhancement of nickel surface concentration for the $LaNiO_3$-600 sample. This ratio is about 4 times higher than that of Ni/La_2O_3, despite the fact that both catalysts have the same nominal Ni loading and were treated under identical conditions. The enhancement of Ni concentration at the surface of the perovskite catalyst is a direct consequence of nickel exsolution upon H_2-activation. The greater surface Ni^0 content of $LaNiO_3$-600 can also be linked to its better CO_2 conversion (Fig. 1).

To further elaborate these findings, photoemission spectra with varied photon energies, thus different analysis depths, were collected in order to distinguish surface from subsurface species. As shown in Fig. 6b and d, the Ni^0 fraction relative to La^{3+} (La_2O_3) decreases in deeper analysis depths for $LaNiO_3$. As it is clearly evident in the HAXPES spectrum for deeper analysis depths (*ca.* 12 nm), Ni^{3+} and La^{3+} components of $LaNiO_3$ are required to properly fit the Ni 2p and La 3d regions. This shows that under the employed conditions, reduction is limited to the outer 2–3 nm and the unreduced perovskite structure is still preserved in the subsurface.

The inverse Ni and La arrangement is noticed for the supported Ni/La_2O_3 catalyst (Fig. 6b and d) with Ni^0 fraction being

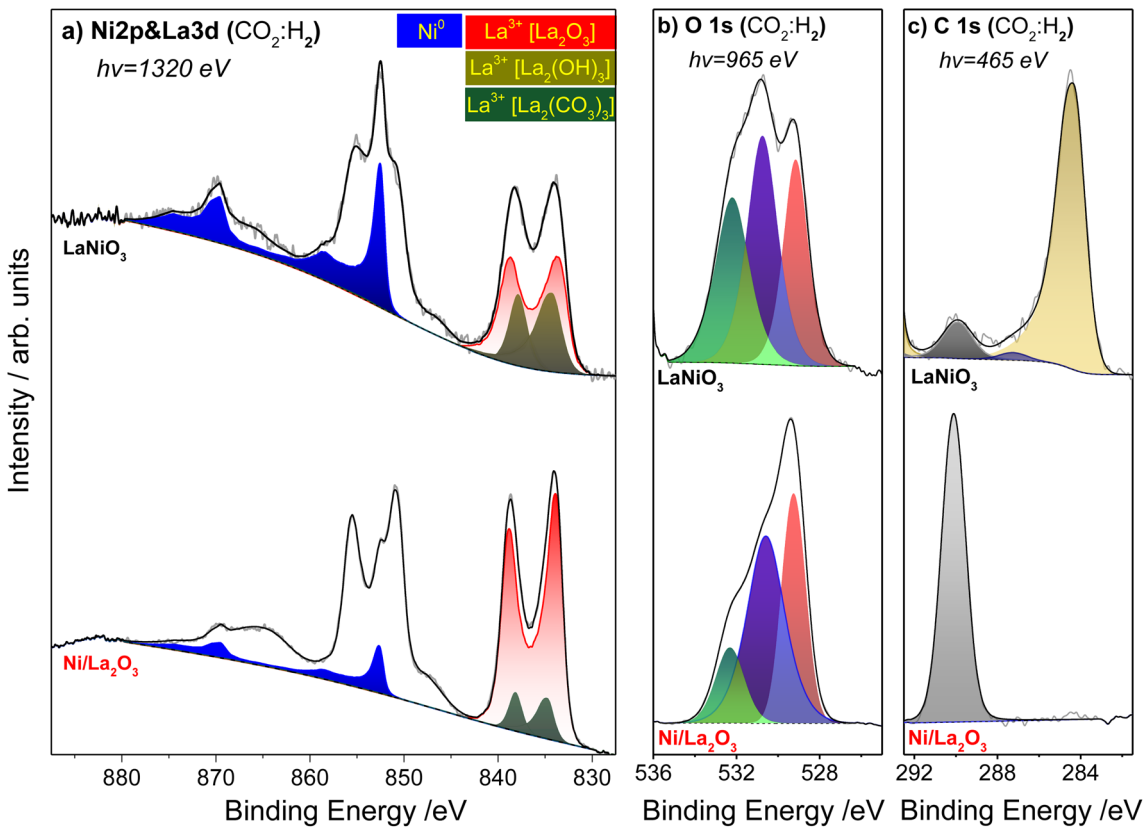

Fig. 7 (a) *In situ* La 3d and Ni 2p AP-XPS spectra of $LaNiO_3$ and Ni/La_2O_3 catalysts under CO_2 methanation conditions (2 mbar CO_2 : H_2 (1 : 1) at 400 °C). Prior to the AP-XPS measurements both catalysts were pre-activated in H_2 at 600 °C. Peak line-shapes derived from reference materials and synthetic line-shapes derived by a mathematical formula are used to fit the La 3d & Ni 2p curves. For clarity only the La $3d_{5/2}$ and Ni 2p fitting components are shown. The corresponding (b) O 1s spectra fitted by three O 1s symmetric peaks and (c) C 1s spectra fitted with asymmetric and symmetric peaks. The estimated information depth (three times the photoelectron inelastic mean free path) is about 4 for La 3d & Ni 2p and O 1s spectra, and 2 nm for C 1s.

low at the outer surface and increasing in deeper layers (up to 20 nm). This trend suggests total or partial Ni encapsulation by lanthana alluding strong metal support interaction (SMSI) phenomena.[64,65] Assuming that the reactivity is proportional to the amount of accessible Ni sites on the surface, increase of Ni surface concentration in the case of $LaNiO_3$ might explain its greater CO_2 methanation activity when compared to Ni/La_2O_3.

3.4. *In situ* AP-XPS/HAXPES investigation under CO_2 hydrogenation conditions

Ex situ TEM/EDX and XAFS analyses of the spent $LaNiO_3$ catalyst do not show any considerable difference with the earlier activated state (Fig. 3 and 4), while XRD indicates that $La_2O_2CO_3$ oxycarbonates are built after long term CO_2 methanation tests (Fig. 2). The surface chemical state, under conditions relevant to CO_2 methanation, was analyzed by AP-XPS. Fig. 7a compares the Ni 2p and La 3d spectra of $LaNiO_3$-600 and Ni/La_2O_3 catalysts measured at 400 °C in 2 mbar $CO_2 : H_2$ (1 : 1). The sharp feature at 855.6 eV suggests that Ni remains metallic in both catalysts similar to the finding in H_2. In contrast, the La $3d_{5/2}$ peak under the reaction conditions is modified as compared to the prior state in H_2 (Fig. S12†). A fitting attempt by the linear combination of $La^{3+}(LaNiO_3)$ and $La^{3+}(La_2O_3)$ reference peak profiles failed to reproduce La $3d_{5/2}$, excluding the possibility that the $La^{3+}(LaNiO_3)$ phase is partially restored during the reaction. The quality of the fitting (*i.e.*, lower STD value) is considerably improved when a synthetic La 3d curve combining 2 pairs of main and satellite peaks is used. More details about this peak, hereafter abbreviated as s.La 3d, are given in Table S2.† The fraction of s.La 3d is more pronounced in $LaNiO_3$ than Ni/La_2O_3 sample. The fit's optimal s.La 3d peak profile exhibited a somewhat different main to satellite peak BE splitting (abbreviated as ΔLa 3d) for the two catalysts. Specifically, ΔLa 3d for $LaNiO_3$ (hereafter s.La 3d($LaNiO_3$)) was 3.6 eV while for Ni/La_2O_3 (hereafter s.La 3d(Ni/La_2O_3)) was 3.4 eV. The ΔLa 3d is very sensitive to the lanthanum chemical state and has been used to distinguish between various lanthanum compounds (Table 3). Accordingly, the ΔLa 3d of s.La 3d($LaNiO_3$) corresponds to hydroxide or carbonate lanthanum species, while s.La 3d(Ni/La_2O_3) primarily to carbonate (*vide infra*). Depth-dependent La 3d measurements (Fig. S13†) reveal possible differences in the location of syn.La 3d between the two catalysts. In particular, for the $LaNiO_3$ catalyst the s.La 3d($LaNiO_3$) fraction is independent of the analysis depth suggesting homogeneous distribution within the outer 4 nm. In contrast, the s.La 3d(Ni/La_2O_3) fraction increases at the surface indicating its preferential location at the outermost surface.

The O 1s and C 1s peaks corroborate the proposed arrangement and provide further details on the chemical nature of the species behind the s.La 3d peaks. The O 1s spectra shown in Fig. 7b are fitted with three O 1s components with BE at 529.2, 530.7 and 532.2 eV (±0.2 eV). The peak at 529.2 eV is typical of La_2O_3 lattice oxygen (abbreviated as O_{lat}),[63,68] while the broad peak at 532.2 eV is probably the convolution of OH^- groups (OH) and carbonates (CO_3^{2-}) both appearing within this energy region.[68] The one at 530.7 eV is more difficult to assign since its BE is relatively low for OH and high for O_{lat} species. Its presence is also clearly manifested in the spectrum measured in an H_2 atmosphere (Fig. S14†). Based on the evolution of the three oxygen species observed in the depth-dependent O 1s measurements (Fig. S15†) their distribution within the outer layers of the catalyst can be determined. Accordingly, the peak at 529.2 eV is located subsurface, while the peak at 532.2 eV is predominantly on the surface. Additionally, the peak at 530.7 eV seems to be distributed rather homogeneously with the analysis depth. The analysis of the Ni/La_2O_3 catalyst gives very similar results, the only difference is that the fraction of O_{lat} on this sample is relatively less.

The C 1s spectrum of $LaNiO_3$ (Fig. 7c) is composed by a main C 1s peak at 284.4 eV typical of C–C and C–H bonds (for simplicity noted as C–C hereafter) and two smaller peaks at 287.3 eV and 289.8 eV assigned to C–O or C=O (C–O hereafter) and carbonate (CO_3^{2-}) species, respectively.[37,63,73] The lack of peaks around 283 eV excludes the presence of Ni-carbides.[37] The C–C peak was present during the H_2 reduction step (Fig. S14†), therefore it is attributed to residual carbon preexisting under the reaction conditions. Depth-dependent C 1s spectra (Fig. S16a†) suggest that CO_3^{2-} is in contact with lanthana beneath a C–C layer. The CO_3^{2-}/s.La 3d($LaNiO_3$) stoichiometry calculated from the corresponding photoemission peaks was 0.1, far below any known La carbonate species. Since extensive La carbonate formation is excluded, $La(OH)_3$ species formation remains the most credible scenario for the origin of s.La 3d($LaNiO_3$). The s.La 3d($LaNiO_3$) value of 3.6 eV discussed above further supports this argument. The evident reason for the formation of $La(OH)_3$ under the reaction conditions and not in

Table 3 The La $3d_{5/2}$ component splitting (ΔLa 3d) for various lanthanum compounds. The standard deviation of the values collected from the cited literature is included in parenthesis

Name	ΔLa 3d (STD) (eV)	Reference
Lanthanum oxide (lanthana) La_2O_3	4.6(±0.3)	63 and 66–68
Lanthanum oxycarbonate $La_2O_2CO_3$	4.3(±0.2)	66, 68 and 69
Lanthanum hydroxide $La(OH)_3$	3.7(±0.3)	63, 66–68, 70 and 71
Lanthanum carbonate $La_2(CO_3)_3$	3.5(±0.1)	70–72
$LaNiO_3$	3.8	This work
La_2O_3	4.7	This work
s.La 3d($LaNiO_3$)	3.6	This work
s.La 3d(Ni/La_2O_3)	3.4	This work

H_2, is the presence of H_2O which is produced by the methanation reaction.

The C 1s of Ni/La_2O_3 catalyst is dominated by the CO_3^{2-} peak at 290.1 eV, while the signal from other components falls to the background level. Depth-dependent C 1s measurements (Fig. S16b†) suggest that CO_3^{2-} is mainly located at the outer surface, which differs from $LaNiO_3$. The CO_3^{2-}/s.La 3d(Ni/La_2O_3) stoichiometry calculated by XPS is around 1.6, in fair agreement with the $La_2(CO_3)_3$ stoichiometry. The above two experimental findings, in addition to ΔLa 3d = 3.4, are sound evidence for $La_2(CO_3)_3$ formation on Ni/La_2O_3 in sharp contrast with $La(OH)_3$ found for $LaNiO_3$.

To summarize, operando NAP-XPS showed that under the reaction conditions Ni is maintained in the metallic state, while new types of lanthanum species are formed. Analysis of the surface sensitive spectroscopic results suggest that the perovskite $LaNiO_3$ catalyst turns into La-hydroxide (probably $La(OH)_3$) while $La_2(CO_3)_3$ is the main species on supported Ni/La_2O_3. The presence of oxycarbonates (*i.e.*, $La_2O_2CO_3$) on Ni/La_2O_3 is unlikely since it is incompatible with both the s.La 3d(Ni/La_2O_3) and the expected compound stoichiometry (0.5 rather than 1.6).

4. Discussion

Catalytic tests of perovskite and supported Ni–La_2O_3 catalysts show that the CO_2 methanation performance is critically affected by the starting material. This might seem surprising since both catalysts have similar Ni loading and surface area, and after activation in H_2 they also show largely similar XRD patterns. One explanation of the superior perovskite-derived Ni–La_2O_3 catalyst performance frequently suggested in the literature[26,31,33] is the creation of highly dispersed nanoparticles socketing into the oxide matrix. Actually, this morphology was also identified in our exsolved perovskite catalyst by TEM/EDX showing the formation of 6 nm Ni particles that resist sintering under the reaction conditions. Although particle size fixation may be a crucial factor in explaining the exsolved $LaNiO_3$ catalyst's long-term stability (Fig. 1b), thorough *in situ* characterization points to significant differences in the surface chemistry of perovskite and supported catalysts that may be responsible for their distinct performances.

In particular, AP-XPS shows that the amount of Ni exposed to the surface might be up to 4 times higher on $LaNiO_3$ than Ni/La_2O_3 (Fig. 6c). Although this can be partly explained by the dispersion of Ni in the two catalysts, depth-dependent AP-XPS and HAXPES measurements revealed an additional clue, the encapsulation of Ni by lanthana, on the line of the well-known SMSI effect. Indeed, the two catalysts have a very different profile of Ni distribution in the outer 10–20 nm (Fig. 6d). This was found during the H_2-activation step but it is also conserved under the reaction conditions as illustrated in Fig. 8. A similar phenomenon has already been observed when Ni/CeO_2 is exposed under reducing conditions and attributed to Ce_2O_3 migration of the reduced oxide to the metal surface.[74] In another example, closer to the materials investigated in this study, a different mechanism was given to explain the covering of Rh particles by La_2O_3.[75,76] As lanthana is much less prone to reduction, a combination of sintering and phase transformation of the support was proposed to explain the encapsulation of Rh during sample preparation, clearly observed by HRTEM measurements. Although we cannot exclude partial lanthana reduction at the extreme surface of Ni/La_2O_3, if it exists it should be very local according to La 3d peak analysis.

However, the configuration of Ni and lanthana at the outer surface is most probably not the only difference between the two catalysts that contributes to their distinct catalytic performance. By careful analysis of photoemission spectra we identify also crucial differences in their surface chemistry. As displayed in Fig. 8, $La(OH)_3$ species can be easily formed at the early reaction stage on the surface of the exsolved $LaNiO_3$ catalyst. In contrast, on supported Ni/La_2O_3 a thin $La_2(CO_3)_3$ layer is evidenced. The latter, being quite stable and inert towards CO_2, can block surface sites with a detrimental effect on the catalytic performance.

It now remains to correlate AP-XPS finding with *ex situ* XRD of the spent catalysts which at a first glance seems quite contradictory. According to AP-XPS, $La(OH)_3$ species are formed

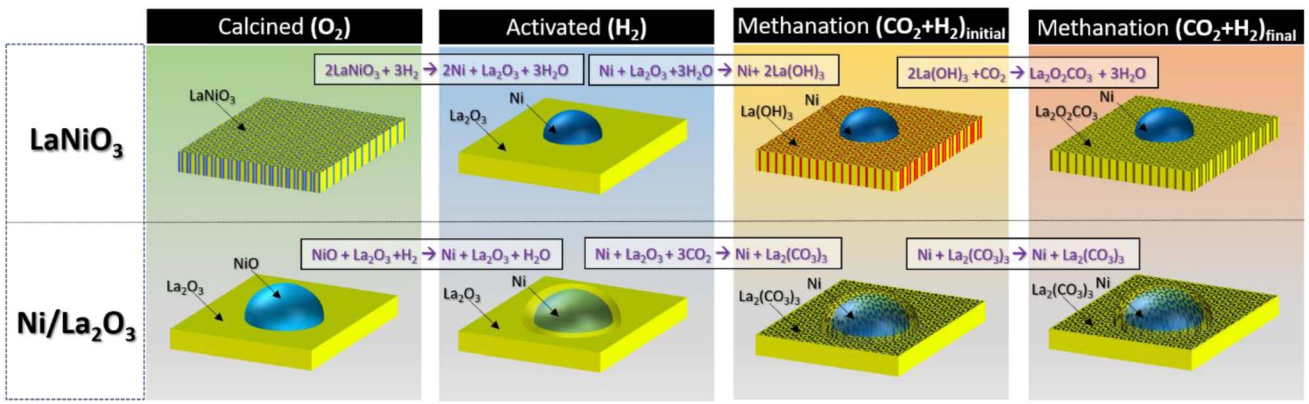

Fig. 8 Illustration of the proposed surface arrangement of $LaNiO_3$ and Ni/La_2O_3 catalysts under calcination, activation and CO_2 methanation (initial and steady state reaction stages) conditions. The proposed surface reactions when the catalysts pass from one condition to the next are shown in boxes.

on the $LaNiO_3$ catalyst under the reaction conditions, but XRD of the spent $LaNiO_3$ show crystalline II-$La_2O_2CO_3$ and not $La(OH)_3$ at all. This might seem even more confusing when one considers results on Ni/La_2O_3 where XRD did not show any additional species after reaction (neither carbonates nor oxycarbonates) despite the fact that the presence of $La_2(CO_3)_3$ was clearly evident in AP-XPS. To explain this, we have to recall first the difference in catalytic reaction conditions between the two experiments. XRD is recorded after 65 hours of reaction at 1 bar, while AP-XPS during 1 hour reaction at 2 mbar total pressure. Evidently, one can anticipate that due to considerably "milder" reaction conditions AP-XPS data represent the initial stages of the catalyst transformation while *ex situ* XRD gives the steady state picture of the catalyst (see Fig. 8). Nevertheless, despite its limitation, AP-XPS remains the best available option to understand the surface chemistry since any *ex situ* XPS analysis will be dubious considering the affinity of lanthana to form carbonates and hydroxides upon exposure to air.

To explain the XRD finding we should extrapolate the AP-XPS data toward the long-term steady state. Indeed, the $La(OH)_3$ species might function as a precursor for $La_2O_2CO_3$. It has been shown that $La(OH)_3$ can be converted to $La_2O_2CO_3$ even after 2 h annealing at 400 °C in air (CO_2 < 0.04% or 0.4 mbar).[77,78] The initial stage of $La_2O_2CO_3$ formation is most probably already observed in the C 1s spectra of $LaNiO_3$ catalyst under the reaction conditions, showing a C 1s peak around 290 eV (Fig. 7c). One can assume that at significantly higher CO_2 concentrations, like in the 1 bar reaction mixture, the $La_2O_2CO_3$ formation rate is enhanced giving rise to the formation of the bulk crystalline $La_2O_2CO_3$ observed in the XRD patterns of Fig. 2a.

The above analysis can also be used to explain the poor catalytic activity of Ni/La_2O_3. In this case $La(OH)_3$, the $La_2O_2CO_3$ precursor, is not readily formed therefore even after hours of reaction oxycarbonates are not observed by XRD. Of course, carbonates may be generated directly by carbonizing La_2O_3 in CO_2 gas, but this requires significantly higher temperatures (*e.g.* 850 °C) than the methanation reaction conditions (350–400 °C).[53] This might suggest that the active state of the exsolved $LaNiO_3$ perovskite catalyst under reforming and methanation conditions could be quite different.

At this stage it is unclear whether the lower CO_2 conversion of Ni/La_2O_3 and the resulting lower production of H_2O is due to the absence of $La(OH)_3$, or if it is an intrinsic characteristic related to the La_2O_3 surface microstructure. As shown earlier, the surface termination plays an important role in lanthana's reactivity with H_2O,[79] suggesting that the surface structure of La_2O_3 is critical in determining whether $La(OH)_3$ forms or not.

The oxycarbonate phases seen in the spent $NiLaO_3$ catalyst have already been observed before on lanthana-based catalysts but were correlated with catalyst deactivation.[80–82] Recently, the presence of $La_2O_2CO_3$ has been claimed to benefit methanation acting as a CO_2 reservoir available for hydrogenation.[83] Our results agree with the latter assessment since the most active and stable sample contained oxycarbonate crystalline phases whereas Ni/La_2O_3 did not. However, the influence of morphological parameters (crystallite size, surface area, Ni dispersion) that could possibly have a role in the reactivity should not be overlooked.[84]

5. Conclusions

$LaNiO_3$ perovskite was synthesized by the Pechini sol gel method and tested in CO_2 methanation after activation by a reductive treatment. The catalytic tests show a net enhancement of the CO_2 conversion with reduction temperature, and superior catalytic performance and stability compared to a Ni/La_2O_3 benchmark catalyst synthesized by conventional wet impregnation. The transformation of the $LaNiO_3$ precursor into the active phase during the thermal reduction treatment was monitored by multiple *ex situ* and *in situ* techniques. Electron microscopy displays the formation of 6 nm Ni particles with narrow size distribution anchored into the La_2O_3 matrix, while *in situ* XAFS detects the intermediate phases of this transition. Although the XRD crystal structures of reduced, exsolved and supported Ni/La_2O_3 seem identical, combined surface/subsurface analysis by *in situ* AP-XPS/HAXPES identified critical differences in the arrangement between La and Ni. Furthermore, it is shown that the active phase is formed during the catalytic cycle and it is quite different from the H_2-activated state. Specifically, although the Ni particle size and oxidation state are maintained, lanthana reacts with the gas phase during the reaction to form new compounds. This information was used to rationalize the differences in the catalytic performance. Notably, encapsulation of Ni by lanthana and the affinity of the latter towards hydroxide or carbonate species formation are proposed to critically affect the catalytic performance. We present strong evidence that the nature of carbon species formed under the reaction conditions is a crucial element of the reactivity, which is promoted by oxycarbonates but suppressed by carbonates. This work highlights the distinct surface chemistry of metal oxide catalysts derived from perovskite precursors in comparison to conventional supported catalysts and extends our understanding on their unique catalytic properties. Differences in the surface chemistry are usually disregarded in the relevant literature, where the high activity and stability of exsolved perovskite catalysts in thermo- or electrochemical reactions are primarily attributed to the socketing of Ni nanoparticles.

Conflicts of interest

There are no conflicts to declare.

Acknowledgements

M. B. and S. Z. acknowledge the support from Strasbourg University and the French Agence Nationale de la Recherche (ANR), under the projects IdEX-2018 (Post-doctorants), DuCaCO$_2$ (No. 236294). J. Z. would like to thank the China Scholarship Council (CSC) for supporting his stay at ICPEES. ESRF is acknowledged for the allocation of synchrotron radiation beamtime and BM23 beamline staff for the collaboration during the experiments. We acknowledge HZB for the allocation

of synchrotron radiation beamtime (proposal no 222-11356-ST) and BESSY Synchrotron staff for the collaboration during the experiments. The authors acknowledge ESRF for beamtime allocation together with Dr K. Lomachenko for support during XAS measurements. A. Molokova is acknowledged for support with development of XAS analysis using Python scripts. Dr A. Martini is acknowledged for providing the EXAFS Wavelet Transform analysis code employed in this work. EB acknowledges support from Project no. 2017KKP5Z PRIN-2017 MOSCATo and Project CH4.0 under the MUR program "Dipartimenti di Eccellenza 2023-2027" (CUP: D13C22003520001). Finally, we thank X. Thanh Nguyen for his considerable contribution to the experiments during his master thesis at ICPEES and Dr S. Labidi for the support with the catalytic measurements.

References

1 Z. Liu, Z. Deng, S. J. Davis, C. Giron and P. Ciais, *Nat. Rev. Earth Environ.*, 2022, **3**, 217–219.
2 International Energy and Agency, 2022, **https://iea.blob.core.windows.net/assets/c3086240-732b-4f6a-89d7-db01be018f5e/GlobalEnergyReviewCO2Emissionsin2021.pdf**, **https://www.iea.org/reports/global-energy-review-c**, Accessed April 22th, 2023.
3 H. S. Whang, J. Lim, M. S. Choi, J. Lee and H. Lee, *BMC Chem. Eng.*, 2019, **1**, 9.
4 J. Ashok, S. Pati, P. Hongmanorom, Z. Tianxi, C. Junmei and S. Kawi, *Catal. Today*, 2020, **356**, 471–489.
5 X. Su, J. Xu, B. Liang, H. Duan, B. Hou and Y. Huang, *J. Energy Chem.*, 2016, **25**, 553–565.
6 C. Vogt, M. Monai, G. J. Kramer and B. M. Weckhuysen, *Nat. Catal.*, 2019, **23**(2), 188–197.
7 P. A. U. Aldana, F. Ocampo, K. Kobl, B. Louis, F. Thibault-Starzyk, M. Daturi, P. Bazin, S. Thomas and A. C. Roger, *Catal. Today*, 2013, **215**, 201–207.
8 A. Cárdenas-Arenas, A. Quindimil, A. Davó-Quiñonero, E. Bailón-García, D. Lozano-Castelló, U. De-La-Torre, B. Pereda-Ayo, J. A. González-Marcos, J. R. González-Velasco and A. Bueno-López, *Appl. Catal., B*, 2020, **265**, 118538.
9 R.-P. Ye, Q. Li, W. Gong, T. Wang, J. J. Razink, L. Lin, Y.-Y. Qin, Z. Zhou, H. Adidharma, J. Tang, A. G. Russell, M. Fan and Y.-G. Yao, *Appl. Catal., B*, 2020, **268**, 118474.
10 W. Li, Y. Liu, M. Mu, F. Ding, Z. Liu, X. Guo and C. Song, *Appl. Catal., B*, 2019, **254**, 531–540.
11 H. Liu, S. Xu, G. Zhou, K. Xiong, Z. Jiao and S. Wang, *Fuel*, 2018, **217**, 570–576.
12 G. Zhou, T. Wu, H. Zhang, H. Xie and Y. Feng, *Chem. Eng. Commun.*, 2014, **201**, 233–240.
13 F. Wang, S. He, H. Chen, B. Wang, L. Zheng, M. Wei, D. G. Evans and X. Duan, *J. Am. Chem. Soc.*, 2016, **138**, 6298–6305.
14 A. Aitbekova, L. Wu, C. J. Wrasman, A. Boubnov, A. S. Hoffman, E. D. Goodman, S. R. Bare and M. Cargnello, *J. Am. Chem. Soc.*, 2018, **140**, 13736–13745.
15 F. Feng, G. Song, J. Xiao, L. Shen and S. V. Pisupati, *Fuel*, 2019, **235**, 85–91.
16 S. Rönsch, J. Schneider, S. Matthischke, M. Schlüter, M. Götz, J. Lefebvre, P. Prabhakaran and S. Bajohr, *Fuel*, 2016, **166**, 276–296.
17 W. Wang, S. Wang, X. Ma and J. Gong, *Chem. Soc. Rev.*, 2011, **40**, 3703–3727.
18 G. Varvoutis, M. Lykaki, S. Stefa, V. Binas, G. E. Marnellos and M. Konsolakis, *Appl. Catal., B*, 2021, **297**, 120401.
19 L. Shen, J. Xu, M. Zhu and Y. F. Han, *ACS Catal.*, 2020, **10**, 14581–14591.
20 C. Vogt, E. Groeneveld, G. Kamsma, M. Nachtegaal, L. Lu, C. J. Kiely, P. H. Berben, F. Meirer and B. M. Weckhuysen, *Nat. Catal.*, 2018, **1**, 127–134.
21 K. Yoshikawa, M. Kaneeda and H. Nakamura, *Energy Procedia*, 2017, **114**, 2481–2487.
22 G. I. Siakavelas, N. D. Charisiou, A. AlKhoori, S. AlKhoori, V. Sebastian, S. J. Hinder, M. A. Baker, I. V. Yentekakis, K. Polychronopoulou and M. A. Goula, *J. CO_2 Util.*, 2021, **51**, 101618.
23 P. H. Ho, G. S. de Luna, S. Angelucci, A. Canciani, W. Jones, D. Decarolis, F. Ospitali, E. R. Aguado, E. Rodríguez-Castellón, G. Fornasari, A. Vaccari, A. M. Beale and P. Benito, *Appl. Catal., B*, 2020, **278**, 119256.
24 G. Tang, D. Gong, H. Liu and L. Wang, *Catalysts*, 2019, **9**, 442.
25 V. Alcalde-Santiago, A. Davó-Quiñonero, D. Lozano-Castelló, A. Quindimil, U. De-La-Torre, B. Pereda-Ayo, J. A. González-Marcos, J. R. González-Velasco and A. Bueno-López, *ChemCatChem*, 2019, **11**, 810–819.
26 K. Kousi, C. Tang, I. S. Metcalfe, D. Neagu, K. Kousi, S. Metcalfe, C. Tang and D. Neagu, *Small*, 2021, **17**, 2006479.
27 Q. Yang, G. Liu and Y. Liu, *Ind. Eng. Chem. Res.*, 2018, **57**, 1–17.
28 K. Kousi, D. Neagu, L. Bekris, E. Calì, G. Kerherve, E. I. Papaioannou, D. J. Payne and I. S. Metcalfe, *J. Mater. Chem. A*, 2020, **8**, 12406–12417.
29 J. Zhang, M. R. Gao and J. L. Luo, *Chem. Mater.*, 2020, **32**, 5424–5441.
30 S. Bhattar, M. A. Abedin, S. Kanitkar and J. J. Spivey, *Catal. Today*, 2021, **365**, 2–23.
31 J. Wu, R. Ye, D. J. Xu, L. Wan, T. R. Reina, H. Sun, Y. Ni, Z. F. Zhou and X. Deng, *Front. Chem.*, 2022, **10**, 961355.
32 O. Kwon, S. Joo, S. Choi, S. Sengodan and G. Kim, *JPhys Energy*, 2020, **2**, 032001.
33 M. A. Salaev, L. F. Liotta and O. V. Vodyankina, *Int. J. Hydrogen Energy*, 2022, **47**, 4489–4535.
34 X. Bao, M. Behrens, G. Ertl, Q. Fu, A. Knop-Gericke, T. Lunkenbein, M. Muhler, C. M. Schmidt and A. Trunschke, *ACS Catal.*, 2021, **11**, 6243–6260.
35 H. S. Lim, G. Kim, Y. Kim, M. Lee, D. Kang, H. Lee and J. W. Lee, *Chem. Eng. J.*, 2021, **412**, 127557.
36 P. Steiger, O. Kröcher and D. Ferri, *Appl. Catal., A*, 2020, **590**, 117328.
37 A. P. Ramon, X. Li, A. H. Clark, O. V. Safonova, F. C. Marcos, E. M. Assaf, J. A. van Bokhoven, L. Artiglia and J. M. Assaf, *Appl. Catal., B*, 2022, **315**, 121528.

38 D. D. Athayde, D. F. Souza, A. M. A. Silva, D. Vasconcelos, E. H. M. Nunes, J. C. D. Da Costa and W. L. Vasconcelos, *Ceram. Int.*, 2016, **42**, 6555–6571.
39 G. Wu, S. Li, C. Zhang, T. Wang and J. Gong, *Appl. Catal., B*, 2014, **144**, 277–285.
40 Y. Gao, D. Chen, M. Saccoccio, Z. Lu and F. Ciucci, *Nano Energy*, 2016, **27**, 499–508.
41 W. Smekal, W. S. M. Werner and C. J. Powell, *Surf. Interface Anal.*, 2005, **37**, 1059–1067.
42 G. Greczynski and L. Hultman, *Angew. Chem., Int. Ed.*, 2020, **59**, 5002–5006.
43 S. Turczyniak, D. Teschner, A. Machocki and S. Zafeiratos, *J. Catal.*, 2016, **340**, 321–330.
44 F. Polack, M. Silly, C. Chauvet, B. Lagarde, N. Bergeard, M. Izquierdo, O. Chubar, D. Krizmancic, M. Ribbens, J. -P. Duval, C. Basset, S. Kubsky and F. Sirotti, *AIP Conf. Proc.*, 2010, **1234**, 185.
45 R. Follath, M. Hävecker, G. Reichardt, K. Lips, J. Bahrdt, F. Schäfers and P. Schmid, *J. Phys.: Conf. Ser.*, 2013, 212003.
46 S. Hendel, F. Schäfers, M. Hävecker, G. Reichardt, M. Scheer, J. Bahrdt and K. Lips, *AIP Conf. Proc.*, 2016, **1741**, 030038.
47 O. Mathon, A. Beteva, J. Borrel, D. Bugnazet, S. Gatla, R. Hino, I. Kantor, T. Mairs, M. Munoz, S. Pasternak, F. Perrin and S. Pascarelli, *J. Synchrotron Radiat.*, 2015, **22**, 1548–1554.
48 D. Bellet, B. Gorges, A. Dallery, P. Bernard, E. Pereiro and J. Baruchel, *J. Appl. Crystallogr.*, 2003, **36**, 366–367.
49 M. Newville, *J. Phys.: Conf. Ser.*, 2013, **430**, 012007.
50 B. Ravel and M. Newville, *J. Synchrotron Radiat.*, 2005, **12**, 537–541.
51 A. Martini, I. A. Pankin, A. Marsicano, K. A. Lomachenko and E. Borfecchia, *Radiat. Phys. Chem.*, 2020, **175**, 108333.
52 A. Quindimil, J. A. Onrubia-Calvo, A. Davó-Quiñonero, A. Bermejo-López, E. Bailón-García, B. Pereda-Ayo, D. Lozano-Castelló, J. A. González-Marcos, A. Bueno-López and J. R. González-Velasco, *J. CO_2 Util.*, 2022, **57**, 101888.
53 A. Olafsen, A. K. Larsson, H. Fjellvåg and B. C. Hauback, *J. Solid State Chem.*, 2001, **158**, 14–24.
54 X. Li, Z. J. Zhao, L. Zeng, J. Zhao, H. Tian, S. Chen, K. Li, S. Sang and J. Gong, *Chem. Sci.*, 2018, **9**, 3426–3437.
55 H. Provendier, C. Petit, C. Estournès, S. Libs and A. Kiennemann, *Appl. Catal., A*, 1999, **180**, 163–173.
56 H. Hojo, Y. Inohara, R. Ichitsubo and H. Einaga, *Catal. Today*, 2023, **410**, 127–134.
57 S. Ramesh and N. J. Venkatesha, *ACS Sustain. Chem. Eng.*, 2017, **5**, 1339–1346.
58 S. Singh, D. Zubenko and B. A. Rosen, *ACS Catal.*, 2016, **6**, 4199–4205.
59 W. Nabgan, T. A. T. Abdullah, R. Mat, B. Nabgan, A. A. Jalil, L. Firmansyah and S. Triwahyono, *Int. J. Hydrogen Energy*, 2017, **42**, 8975–8985.
60 P. Cao, P. Tang, M. F. Bekheet, H. Du, L. Yang, L. Haug, A. Gili, B. Bischoff, A. Gurlo, M. Kunz, R. E. Dunin-Borkowski, S. Penner and M. Heggen, *J. Phys. Chem. C*, 2022, **126**, 786–796.
61 G. Agostini, A. Piovano, L. Bertinetti, R. Pellegrini, G. Leofanti, E. Groppo and C. Lamberti, *J. Phys. Chem. C*, 2014, **118**, 4085–4094.
62 D. Salusso, E. Borfecchia and S. Bordiga, *J. Phys. Chem. C*, 2021, **125**, 22249–22261.
63 M. F. Sunding, K. Hadidi, S. Diplas, O. M. Løvvik, T. E. Norby and A. E. Gunnæs, *J. Electron Spectrosc. Relat. Phenom.*, 2011, **184**, 399–400.
64 P. Petzoldt, M. Eder, S. Mackewicz, M. Blum, T. Kratky, S. Günther, M. Tschurl, U. Heiz and B. A. J. Lechner, *J. Phys. Chem. C*, 2022, **126**, 16127–16139.
65 C. J. Pan, M. C. Tsai, W. N. Su, J. Rick, N. G. Akalework, A. K. Agegnehu, S. Y. Cheng and B. J. Hwang, *J. Taiwan Inst. Chem. Eng.*, 2017, **74**, 154–186.
66 Y. Pang, X. Zhou, E. I. Vovk, C. Guan, S. Li, A. P. van Bavel and Y. Yang, *Appl. Surf. Sci.*, 2021, **548**, 149214.
67 S. Mickevičius, S. Grebinskij, V. Bondarenka, B. Vengalis, K. Šliužiene, B. A. Orlowski, V. Osinniy and W. Drube, *J. Alloys Compd.*, 2006, **423**, 107–111.
68 J. P. H. Li, X. Zhou, Y. Pang, L. Zhu, E. I. Vovk, L. Cong, A. P. Van Bavel, S. Li and Y. Yang, *Phys. Chem. Chem. Phys.*, 2019, **21**, 22351–22358.
69 W. Gu, J. Liu, M. Hu, F. Wang and Y. Song, *ACS Appl. Mater. Interfaces*, 2015, **7**, 26914–26922.
70 D. R. Inns, X. Pei, Z. Zhou, D. J. M. Irving and S. A. Kondrat, *Mater. Today Chem.*, 2022, **26**, 101230.
71 D. R. Inns, A. J. Mayer, V. Skukauskas, T. E. Davies, J. Callison and S. A. Kondrat, *Top. Catal.*, 2021, **64**, 992–1009.
72 X. Zhou, Y. Pang, Z. Liu, E. I. Vovk, A. P. van Bavel, S. Li and Y. Yang, *J. Energy Chem.*, 2021, **60**, 649–659.
73 L. Zhong, M. Barreau, V. Caps, V. Papaefthimiou, M. Haevecker, D. Teschner, W. Baaziz, E. Borfecchia, L. Braglia and S. Zafeiratos, *ACS Catal.*, 2021, **11**, 5369–5385.
74 M. Li and A. C. van Veen, *Appl. Catal., B*, 2018, **237**, 641–648.
75 S. Bernal, J. J. Calvino, M. A. Cauqui, J. M. Gatica, C. López Cartes, J. A. Pérez Omil and J. M. Pintado, *Catal. Today*, 2003, **77**, 385–406.
76 S. Bernal, J. J. Calvino, C. López-Cartes, J. M. Pintado, J. A. Pérez-Omil, J. M. Rodríguez-Izquierdo, K. Hayek and G. Rupprechter, *Catal. Today*, 1999, **52**, 29–43.
77 G. Chen, B. Han, S. Deng, Y. Wang and Y. Wang, *Electrochim. Acta*, 2014, **127**, 355–361.
78 D. Ding, W. Lu, Y. Xiong, X. Pan, J. Zhang, C. Ling, Y. Du and Q. Xue, *Appl. Surf. Sci.*, 2017, **426**, 725–733.
79 K. A. Stoerzinger, R. Comes, S. R. Spurgeon, S. Thevuthasan, K. Ihm, E. J. Crumlin and S. A. Chambers, *J. Phys. Chem. Lett.*, 2017, **8**, 1038–1043.
80 H. Chen, H. Yu, F. Peng, H. Wang, J. Yang and M. Pan, *J. Catal.*, 2010, **269**, 281–290.
81 L. M. Cornaglia, J. Múnera, S. Irusta and E. A. Lombardo, *Appl. Catal., A*, 2004, **263**, 91–101.
82 X. E. Verykios, *Int. J. Hydrogen Energy*, 2003, **28**, 1045–1063.
83 Y. Dai, M. Xu, Q. Wang, R. Huang, Y. Jin, B. Bian, C. Tumurbaatar, B. Ishtsog, T. Bold and Y. Yang, *Appl. Catal., B*, 2020, **277**, 119271.
84 R. P. Turcotte, J. O. Sawyer and L. Eyring, *Inorg. Chem.*, 1969, **8**, 238–246.